SPECIAL
DIAMET
COLLECTION

Diabatic Heating and Cooling Rates Derived from In Situ Microphysics Measurements: A Case Study of a Wintertime U.K. Cold Front

C. DEARDEN, P. J. CONNOLLY, G. LLOYD, J. CROSIER, K. N. BOWER, T. W. CHOULARTON, AND G. VAUGHAN

Centre for Atmospheric Science, University of Manchester, Manchester, United Kingdom

(Manuscript received 5 February 2014, in final form 17 April 2014)

ABSTRACT

In situ measurements associated with the passage of a kata cold front over the United Kingdom on 29 November 2011 are used to initialize a Lagrangian parcel model for the purpose of calculating rates of diabatic heating and cooling associated with the phase changes of water within the cloud system. The parcel model calculations are performed with both bin-resolved and bulk treatments of microphysical processes. The in situ data from this case study reveal droplet number concentrations up to 100 cm^{-3}, with planar ice crystals detected at cloud top, as well as columnar crystals produced by rime splinter ejection within the prefrontal warm sector. The results show that in terms of magnitude, the most significant rates of diabatic heating and cooling are produced by condensation growth of liquid water within the convective updrafts at the leading edge of the front. The peak temperature tendencies associated with condensation are typically found to be at least an order of magnitude larger than those associated with the ice phase, although the cooling effect from sublimation and melting occurs over a wide region. The parcel model framework is used in conjunction with the observations to assess the suitability of existing bulk microphysical treatments, of the kind used in operational weather forecast models. It is found that the assumption of spherical ice crystals (with diameters equal to the maximum dimension of those sampled), along with the use of negative exponential functions to describe ice particle size distributions, can lead to an overestimation of local diabatic heating and cooling rates by a factor of 2 or more.

1. Introduction

Microphysical processes involving a phase change of water have the potential to modify cyclonic development through the effects of latent heating and cooling (Manabe 1956; Danard 1964), which can be understood in terms of the diabatic generation of potential vorticity (PV; Hoskins et al. 1985; Stoelinga 1996). However such microphysical–dynamical feedbacks are often difficult to isolate in the midlatitudes given the complex three-dimensional structure and evolution of cyclonic systems. Numerical models are a useful tool to help isolate such diabatic effects, as most recently demonstrated by Joos and Wernli (2012), but uncertainty remains as to how appropriate the microphysics parameterizations employed in such models are, particularly with regards to the ice phase. The evolution of the ice phase is complicated by the dependency of ice crystal habit on both temperature and supersaturation (e.g., Bailey and Hallett 2009), and this subsequently influences the growth rate of ice crystals by both diffusion of water vapor (Fukuta and Takahashi 1999) and collection processes (e.g., Mason 1994). The variations in ice crystal habit and density also affect fall speeds (e.g., Locatelli and Hobbs 1974, hereafter LH74), which in turn affect rates of sublimation and the associated

Denotes Open Access content.

Corresponding author address: Chris Dearden, Centre for Atmospheric Science, Room 3.16, Simon Building, Oxford Road, University of Manchester, Manchester M13 9PL, United Kingdom. E-mail: christopher.dearden@manchester.ac.uk

DOI: 10.1175/MWR-D-14-00048.1

Publisher's Note: This article was revised on 10 November 2014 to include the CCBY license designation that was missing when originally published.

profile of latent cooling. Thus, observations of the microphysics of frontal cloud systems are key to help advance our understanding and to constrain and inform the development of numerical models for use in the midlatitudes.

The Diabatic Influences on Mesoscale Structures in Extratropical Storms (DIAMET) project (Vaughan et al. 2014) conducted four U.K.-based field campaigns between September 2011 and August 2012, which provided a comprehensive set of both in situ and ground-based radar measurements in relation to the microphysics and dynamics of a variety of frontal systems. These measurements are used in combination with numerical models to improve our understanding of the way mesoscale structures develop and give rise to severe weather in extratropical cyclones, and to help improve the prediction of such features in weather forecast models. Cold fronts in particular make suitable case studies since they are typically associated with high-impact mesoscale weather events [e.g., narrow cold frontal rainbands (NCFRs), strong surface wind gusts, and even tornadoes, features that are difficult to forecast accurately]. NCFRs have received considerable attention in the literature over the past few decades. Hobbs and Persson (1982) presented comprehensive observations of an NCFR, a case study later explored in more detail by Rutledge and Hobbs (1984). They suggested that the most intense regions of precipitation within the NCFR (henceforth referred to as precipitation cores) are associated with melting graupel, produced initially by snow crystals collecting liquid drops as they fall (riming). Such work was later complemented by the idealized, steady-state modeling studies of Cox (1988) and Marécal et al. (1993). These studies were based on real case studies from the Cyclonic Extratropical Storms (CYCLES) and Mesoscale Frontal Dynamics Project (MFDP)/FRONTS 87 field campaigns, and both sets of results supported the suggestion that ice phase processes make an important contribution to the distribution and intensity of the precipitation bands, with the Marécal et al. study confirming that graupel was necessary to reproduce the observed precipitation rates. Both studies attempted to quantify the magnitude of the associated latent heating and cooling rates from the simulated microphysics in an attempt to identify the key processes that could impact mesoscale dynamics.

Other studies have used PV inversion techniques to ascertain the impact of diabatic processes on the intensity of mesoscale features. For instance, the cold frontal case study by Lackmann (2002) showed that latent heating produced PV anomalies that modified the mesoscale flow in such a way as to strengthen the low-level jet. Forbes and Clark (2003) also investigated the role of diabatic processes in cold frontal rainbands, with a focus on the ice phase. Their mesoscale model simulations demonstrated the importance of fall speed relationships in determining the vertical profile of latent cooling associated with sublimating ice crystals, and how this affected the morphology of frontal rainbands. Very recently, the in situ microphysics measurements presented in Crosier et al. (2014) and Lloyd et al. (2014) have highlighted the importance of rime splintering (Hallett and Mossop 1974) as a powerful mechanism for secondary ice crystal production in midlatitude cyclones, while also noting the apparent lack of graupel particles despite the high precipitation rates. These findings raise questions concerning the contribution of secondary ice in NCFRs to precipitation formation and how the resultant redistribution of water within the cloud system can affect its mesoscale evolution. Such questions are particularly relevant given that some microphysics schemes used in operational models—for example, the Consortium for Small-Scale Modeling (COSMO; Doms et al. 2007) and the Met Office Unified Model (Wilson and Ballard 1999, hereafter WB99)—do not presently include parameterizations of secondary ice production.

In this paper we use in situ microphysics measurements, in conjunction with a Lagrangian parcel model, to diagnose instantaneous rates of latent heating and cooling associated with a cold front that crossed the United Kingdom on 29 November 2011 (DIAMET intensive observation period 5). The aim is twofold: 1) to elucidate the key microphysical processes involved that could potentially be important in diabatic PV generation; and 2) to identify any weaknesses associated with existing bulk microphysics parameterizations of such processes and to suggest potential ways to improve them where possible. To achieve both these aims, we initialize the parcel model using aircraft measurements of particle size distributions and dynamic/thermodynamic quantities as detailed in section 4a. We perform the parcel model integrations using both explicit (bin) and parameterized (bulk) representations of microphysical processes, where the bin parcel model is used as a benchmark to validate the performance of the bulk scheme. Bin microphysics schemes are currently too expensive for use in operational forecast models, but the approach taken here provides an adequate framework within which to run the bin and bulk schemes in parallel to each other and to then assess the accuracy of the latent heating and cooling rates produced by the latter. By initializing the parcel model with real data obtained from aircraft observations, we bypass many of the uncertainties in the treatment of droplet activation and ice nucleation inherent to cloud microphysics models, allowing us to focus on the validity of the underlying assumptions made in bulk microphysics schemes.

We begin with a general overview of the data collection methods employed during DIAMET in section 2, and then proceed to review the meteorological situation for this

particular case study in section 3. A detailed discussion of the Lagrangian parcel model is presented in section 4, before the results from the parcel modeling are shown in section 5. In section 6, we discuss the potential implications of the diabatic effects of the microphysical processes in terms of the mesoscale evolution of the frontal rainband, while the main conclusions of the paper, along with recommendations for future work, are summarized in section 7.

2. Measurement capability during the DIAMET field campaign

In situ measurements for DIAMET were provided by a modified BAe Systems 146–301 Atmospheric Research Aircraft (henceforth referred to as the "BAe 146"), maintained by the Facility for Airborne Atmospheric Measurement (FAAM) based at Cranfield University, Bedfordshire, United Kingdom. FAAM is jointly run by the U.K. Natural Environment Research Council (NERC) and the Met Office. The BAe 146 is a state-of-the-art airborne laboratory, fitted with a comprehensive set of meteorological probes and microphysics instrumentation to provide measurements of both liquid and ice particles across a range of sizes [see Vaughan et al. (2014) for the DIAMET payload]. For this study, we use data from the Cloud Droplet Probe (CDP), manufactured by Droplet Measurement Technologies (DMT), which uses 30 size bins to sample liquid droplets from 2 up to 50 μm in diameter. Ice particle size distributions (PSDs) are constructed using data from the DMT cloud imaging probe (CIP)-15 and CIP-100 probes. The CIP-15 has a maximum detectable size of 930 μm and a bin width of 15 μm. For larger hydrometeors we use the CIP-100, which has a lower bin resolution of 100 μm but can detect precipitation particles up to 6.2 mm. Both CIP probes were fitted with antishatter tips for the DIAMET campaign, and so contamination of the data by shattering of cloud particles on probe inlets was minimized. We also use detailed images from the SPEC-INC 2D-S probe to help identify the habit (shape) of ice crystals. In terms of phase partitioning, processing software for the CIP-15 (CIP-100) is used to distinguish ice crystals from liquid drops at sizes above 45 (400) μm; we still count particles below these sizes, but cannot reliably determine their phase. Consequently, smaller particles are not included in this study unless explicitly stated. For further details of these instruments and the processing of the data, the reader is referred to Lloyd et al. (2014) and Crosier et al. (2014). By merging data from the CIP-15 and CIP-100 probes we were able to construct ice PSDs from 45 μm up to 6.2 mm. We did notice an occasional problem with phase misclassification during the processing of the in situ data; this occurred only in the presence of drizzle drops (i.e., a few hundred micrometers in diameter) which sometimes appear slightly stretched or out of focus, and appear to the processing software as solid. This problem was mainly confined to data collected close to the freezing level; the reader is referred to section 5d for further details.

Ground-based remote sensing data were provided by the Chilbolton Facility for Atmospheric and Radio Research (CFARR) based in Hampshire, United Kingdom. CFARR operate a number of radars; the most relevant instrument for this study is the steerable S-band Chilbolton Advanced Meteorological Radar (CAMRa), a 25-m dish sensitive to cloud and precipitation particles. We use the data from CAMRa to locate the aircraft with respect to the frontal system, and also to provide insight into the mesoscale evolution of the cross-frontal flow.

3. Meteorological overview of the case study

Figure 1 shows the synoptic surface pressure chart valid at 1200 UTC 29 November 2011, with a low pressure center to the northeast of Iceland, and the associated cold front extending down across the length of the United Kingdom, advancing from the west. Met Office rainfall radar maps (Fig. 2) reveal the evolution of a well-defined NCFR as the cold front passed over the United Kingdom, with evidence of clearly identifiable precipitation cores embedded within it. The frontal passage was associated with precipitation rates above 32 mm h^{-1}. Two flights of the BAe 146 were conducted on this day to sample the cold frontal cloud band; the first flight occurred in the morning over the southwest approaches (take off at 0807 UTC). Following landing and refuel in Exeter around 1300 UTC, the aircraft took off again at 1407 UTC and proceeded to fly legs back and forth along the 253° radial from CFARR to Exeter while the front was over land, before landing back at Exeter at 1610 UTC. The flight track is illustrated in Fig. 3. In the morning section of the flight, the aircraft spent significant amounts of time out of clouds because of the patchy nature of the frontal cloud within this area. The afternoon flight legs were more successful and were conducted in tandem with the CAMRa radar at CFARR, which performed continual range–height indicator (RHI) scans along the radial while the aircraft was in flight. Consequently for this paper we concentrate our analysis on the data collected during the afternoon flight. Lloyd et al. (2014) present evidence to suggest that the front underwent a transition from ana to kata type (Bergeron 1937; Sansom 1951; Browning and Monk 1982) as a result of dry air from the upper troposphere descending and crossing ahead of the front, with cloud-top temperatures

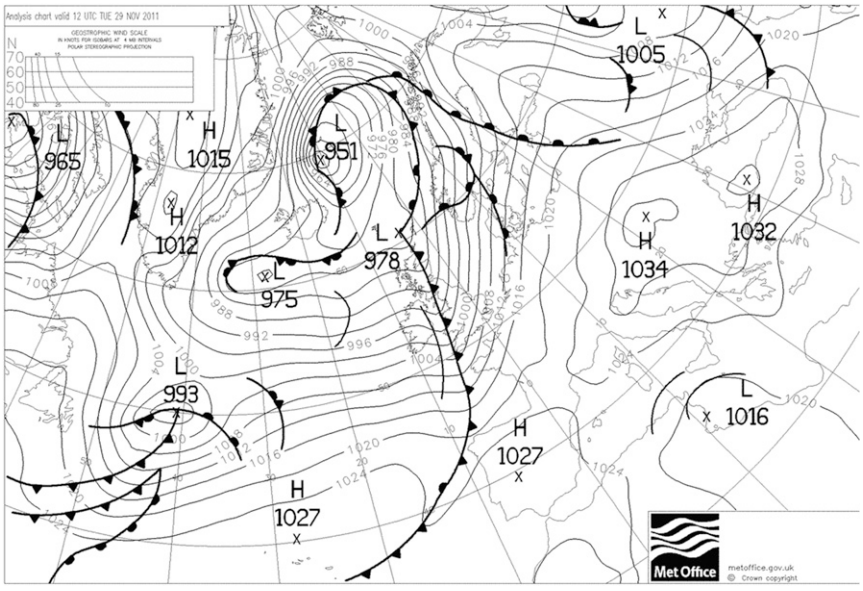

FIG. 1. Met Office surface analysis chart, valid at 1200 UTC 29 Nov 2011 (copyright of the Met Office).

increasing significantly from −40° to approximately −15°C between the morning and afternoon flights.

Observations from the surface meteorological station at CFARR plotted in Fig. 4 reveal that the surface cold front reached Chilbolton at 1600 UTC as indicated by the clear drop in temperature at this time, marking the transition from the warm sector to postfrontal air. The precipitation occurred ahead of the front, supporting the interpretation that it had by this stage completed the transition from ana to kata type. Interestingly, the accompanying pressure trough and shift in wind direction also precede the temperature drop by some 30 min to an hour. The general conceptual understanding is that the pressure minimum and wind shift coincide with the drop in surface temperature; however, many exceptions to this behavior have been noted. These exceptions are consolidated and reviewed by Schultz (2005), who presents mechanisms that can account for such prefrontal troughs and wind shifts; of these, two explanations could apply to the present case, both of which are diabatic in nature. The first is the effect of latent cooling arising from subcloud evaporation of hydrometeors associated with the prefrontal precipitation. The second is the effect of surface friction, which slows down the advection of cold air at the surface, resulting in a nose of cold sector air that overhangs the surface front and arrives ahead of it. The resulting increase in surface pressure would then be due to the denser cold air overrunning the lighter prefrontal air.

A detailed discussion of the microphysics observations for this case study are presented in Lloyd et al. (2014); for brevity only the key points are summarized here. The droplet number concentrations from the afternoon flight were quite low, peaking at 100 cm^{-3} within the region of strong vertical motion at the frontal boundary, indicating a relatively clean air mass. In contrast the ice crystal number concentrations were relatively high for this temperature regime (peaks up to 100 L^{-1}), which are attributed to secondary ice production via rime splintering. The secondary ice columns were mainly confined to the cloudy region in the prefrontal warm sector, whereas at cloud top ice crystal concentrations were much lower, typically 1 L^{-1}, believed to have formed via primary nucleation. Supercooled liquid water was measured near cloud top, corresponding to a temperature of around −15°C. This is consistent with previous ground-based measurements of layer clouds (e.g., Westbrook and Illingworth 2011, and references therein). Table 1 provides a summary of the most interesting legs of the flight; these are the legs on which we will concentrate in the subsequent analysis.

4. Methodology for calculating diabatic effects from in situ microphysics measurements

a. *The Lagrangian parcel model*

The calculation of diabatic heating and cooling rates associated with the processes of condensation, deposition, and riming along the aircraft flight track is achieved using a Lagrangian parcel model constrained directly from the in situ measurements. Parcel model integrations are performed at 1-s intervals along the flight

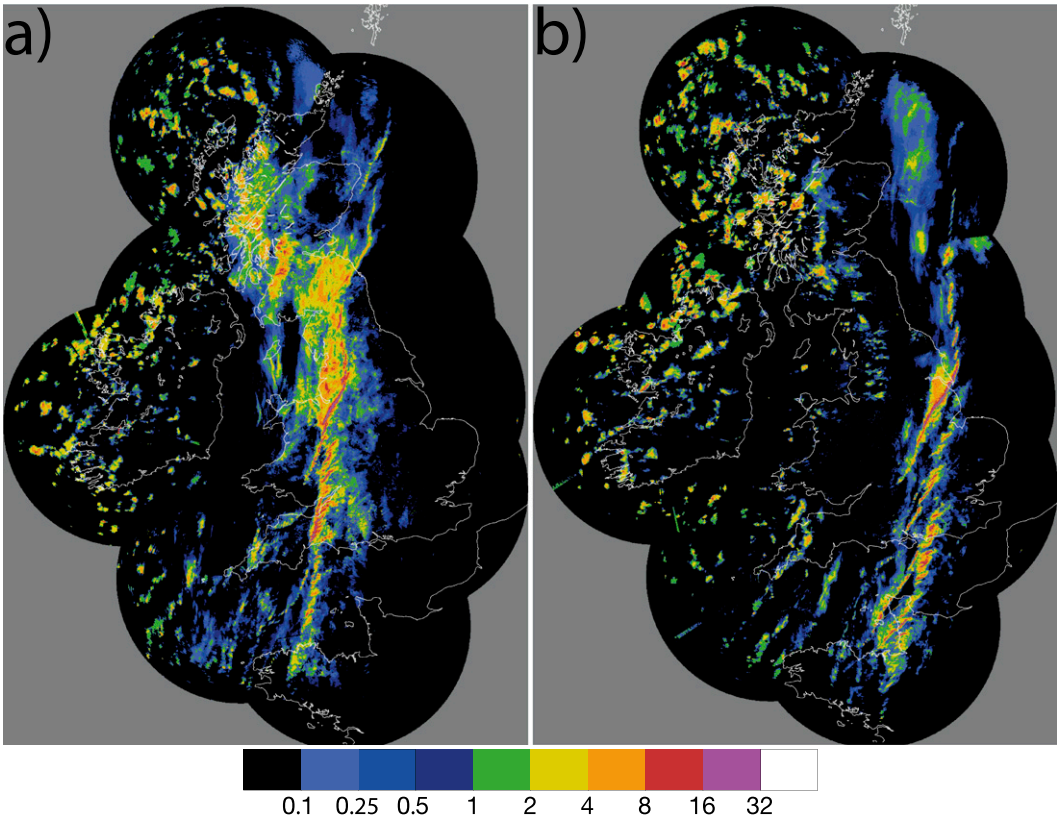

FIG. 2. Precipitation rate (mm h^{-1}) from the Met Office rainfall radar network (1-km composite), at (a) 1400 and (b) 1615 UTC 29 Nov 2011, showing the passage of the narrow cold frontal rainband as it moved eastward across the United Kingdom. These times approximately correspond to the take-off and landing times of the aircraft during the second leg of flying, and so are a fair representation of the distance traveled by the frontal system while the aircraft was in flight (copyright of the Met Office).

track, initialized with 1-Hz measurements of vertical velocity, temperature, pressure, and water vapor mixing ratio (used to calculate relative humidity), assuming that the vertical wind is held constant during each model integration. Since we are interested in calculating instantaneous rates, we use a short integration time of 10 s, although for condensation growth the droplet number concentrations were sometimes sufficiently low that it

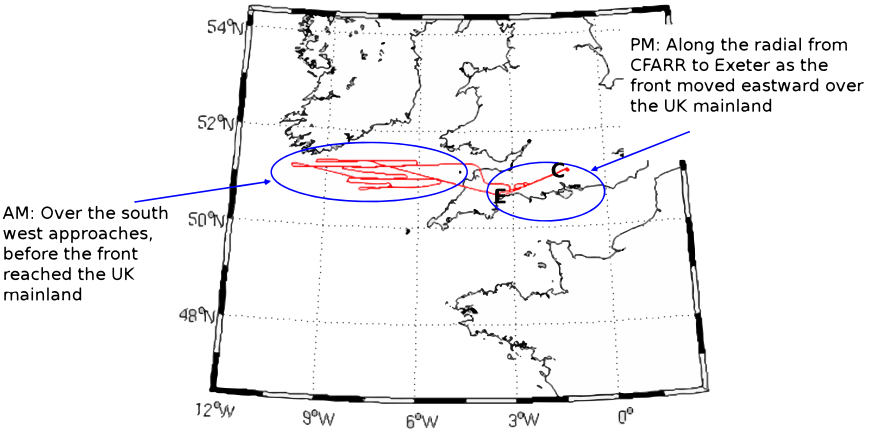

FIG. 3. Map showing the aircraft flight track in red for both the morning and afternoon flights on 29 Nov 2011. The labels "E" and "C" refer to the locations of Exeter and CFARR, respectively. The southwest approaches refers to the region of sea off the south coast of Ireland.

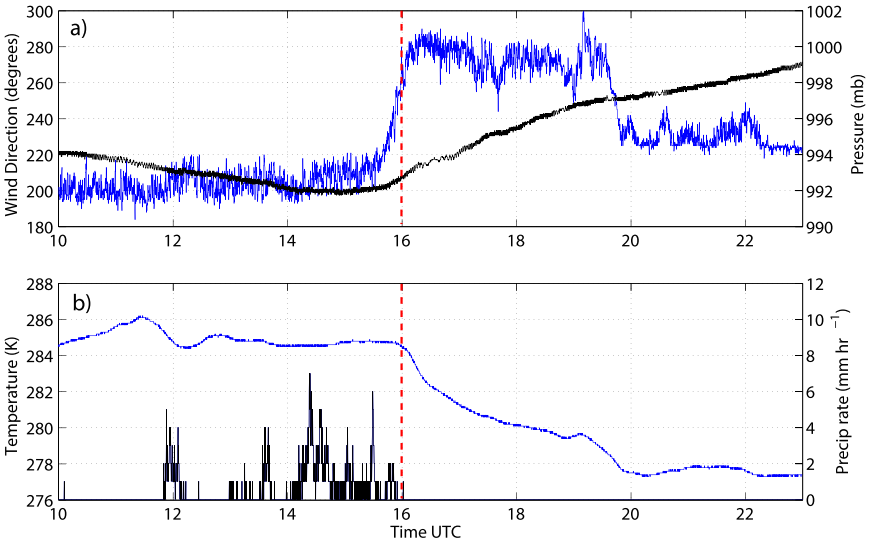

FIG. 4. Selected meteorological variables as measured at the CFARR meteorological station between 1000 and 2300 UTC 29 Nov 2011. (a) Surface wind direction (blue) and pressure (black); (b) surface temperature (blue) and precipitation rate (black). The red dashed line in each plot represents the time at which the surface cold front reached CFARR, based on the change in surface temperature.

was necessary to extend this to 100 s to allow the model to reach a quasi-steady equilibrium supersaturation. The model solves a set of differential equations representing the thermodynamic and microphysical evolution of the air parcel; this is done using the Ordinary Differential Equation (ODE) "ode15s" solver in MATLAB (Shampine and Reichelt 1997). Differential equations representing the change in pressure of the air parcel and the resultant change in temperature are based on hydrostatic balance and the first law of thermodynamics, respectively. Changes in the partitioning of water between the liquid, ice, and vapor phases, and the change in air parcel temperature

TABLE 1. Summary of the most microphysically relevant flight legs between 1410 and 1600 UTC.

Leg	Time (UTC)	Direction along radial relative to Chilbolton	Temperature	Location of aircraft with respect to frontal system	Summary of observed microphysics
Run 10	1414–1426	Inbound straight and level from west	Just below freezing level	Through the frontal rainband and into shallower cloud ahead of surface cold front	Liquid with ice falling from above
Profile 11	1510–1515	Outbound descent from cloud top to cloud base	267–275 K	In the warm sector ahead of surface cold front	Evidence of Hallett–Mossop splinters
Run 13	1515–1521	Outbound straight and level along cloud base	274–271 K	Flew through convective feature at leading edge of front	Large jump in liquid water content in region of high w
Run 14	1527–1537	Inbound straight and level just below cloud top	265–266 K	Transitioning from stratiform region to top of convective cells	Brief period of primary ice (large dendrites and aggregates) at 1528 UTC
Profile 13	1542–1545	Outbound descent from cloud top to middle of cloud	266–268 K	In the warm sector ahead of surface cold front	Evidence of Hallett–Mossop splinters
Run 15	1545–1557	Outbound straight and level, middle of cloud	268 K initially, dropping to 265 K	In the cloudy region behind the main convective rainband	Evidence of sublimating ice crystals

due to the effects of latent heating and cooling, depend on the choice of microphysical representations used in the model [i.e., either explicit (bin resolved) or parameterized (bulk)]. In both cases, the parcel model uses prognostic equations to describe the evolution of liquid and ice in terms of both mass and number. The model microphysical variables are initialized using PSDs constrained directly from data collected by the aircraft as discussed in section 2. It should be noted that the model does not consider the effects of new cloud particle formation from aerosols, and looks solely at the evolution of the measured PSDs due to vapor diffusion and riming. In the case of the bin microphysics scheme, the liquid bins are discretized by dimension with a size range and bin width chosen to match that of the CDP probe. Similarly, the number and width of the ice size bins match those of the cloud probe from which the size distributions were taken (i.e., either CIP-15 or CIP-100, or a composite of the two). For the bulk microphysics, we fit gamma and negative exponential functions to the measured droplet and ice size distributions, respectively, based on the method of moment-conserving fits (Dearden et al. 2011; Connolly et al. 2012).

For each parcel model integration, the ODE solver is set to output values for each prognostic variable at 1-s intervals. The change in mass of liquid or ice over the 10-s integration period is used to compute an average mass mixing ratio tendency dq/dt (in kg kg^{-1} s^{-1}; note that when a 100-s integration time is used for condensation, we calculate the average mass mixing ratio tendency from the final 10 s of integration). Rates of change of mass are then converted to instantaneous heating rates, dT/dt, thus,

$$\left.\frac{dT}{dt}\right|_{\text{con}} = \left.\frac{dq}{dt}\right|_{\text{con}} \frac{L_v}{\text{cp}_m}, \tag{1a}$$

$$\left.\frac{dT}{dt}\right|_{\text{dep}} = \left.\frac{dq}{dt}\right|_{\text{dep}} \frac{L_s}{\text{cp}_m}, \quad \text{and} \tag{1b}$$

$$\left.\frac{dT}{dt}\right|_{\text{rim}} = \left.\frac{dq}{dt}\right|_{\text{rim}} \frac{L_f}{\text{cp}_m}. \tag{1c}$$

The subscripts con, dep, and rim refer to the processes of condensation, deposition, and riming, respectively; L_v, L_s, and L_f are the latent heat coefficients for vaporization, sublimation, and fusion; and cp_m is the specific heat of moist air at constant pressure.

Where appropriate, cooling rates due to melting are also calculated, although rates of change of ice mass due to melting are not computed using the parcel model framework; instead we simply use in situ microphysics measurements along a straight and level run at the top of the melting layer to calculate the flux of falling ice, assuming that the melting occurs within a layer of depth Δz (see section 5d). This yields an expression for the rate of change of ice mass due to melting, $dq/dt|_{\text{mlt}}$, which we then use to calculate the corresponding cooling rate:

$$\left.\frac{dT}{dt}\right|_{\text{mlt}} = \left.\frac{dq}{dt}\right|_{\text{mlt}} \frac{L_f}{\text{cp}_m}. \tag{2}$$

Full details of the bin and bulk microphysical representations used in the parcel model are given in the appendix. In our growth rate calculations, no mixing of environmental air into the parcel is assumed, because reliable rates of entrainment and mixing cannot be easily constrained from the available observations. We highlight the neglect of mixing effects as a caveat here, although given the relatively short integration times of the parcel model we believe that their omission will not have a significant effect on our conclusions.

The condensation and deposition growth terms used in the model require knowledge of the relative humidity of the environment and the vertical velocity of the air. For liquid and mixed-phase cloud, we assume that the air parcel starts from water saturation. The aircraft was fitted with a turbulence probe to measure vertical velocity (although there were periods during this flight when the probe was affected by icing problems in mixed-phase cloud). For ice-only conditions, we cannot assume ice saturation as an initial condition and so we use hygrometer data from the aircraft to calculate the relative humidity of the ambient air with respect to ice. The aircraft was fitted with three different hygrometer probes for DIAMET: two chilled mirror instruments—the General Eastern and the Buck Research Instruments CR-2 (henceforth referred to as the GE and Buck, respectively)—and a tunable diode laser instrument, the WVSS-II (Vance et al. 2011), the reliability of which we now discuss.

b. Intercomparison of hygrometer data

Figure 5a compares the water vapor mixing ratio measurements from each of the hygrometers on board the aircraft for this flight, as a function of flight time. Initially the Buck overreads considerably compared to the other two probes; this is most likely due to the common problem of condensation forming within the instrument body (A. Woolley, FAAM, 2012, personal communication), particularly since the aircraft had already spent considerable time at altitude during the morning flight and any condensation may not have fully evaporated before the afternoon flight began. The agreement between the remaining probes, the WVSS-II and the GE, is for the most part very good. There is a

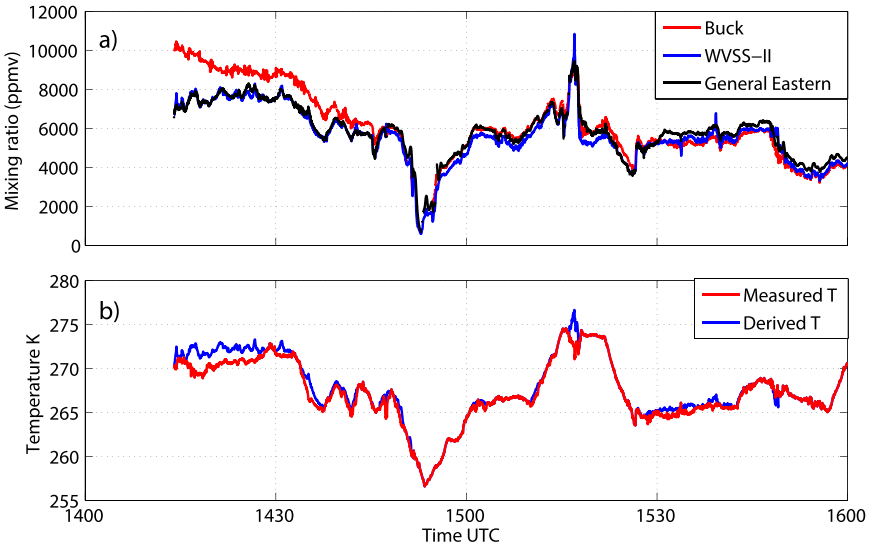

FIG. 5. (a) Comparison of water vapor mixing ratio measurements from the hygrometer probes on board the aircraft for the afternoon flight on 29 Nov 2011; (b) in situ measurements of ambient temperature from the aircraft de-iced temperature probe (red) and derived temperature within liquid and mixed-phase cloud using WVSS-II data (blue).

tendency for the GE to overread slightly relative to the WVSS-II beyond 1500 UTC, likely to be due to a problem with water ingress on the GE probe when operating in cloud. Since the WVSS-II uses a tunable laser diode, with a faster response time than the chilled mirror instruments and without the issues of water ingress, this instrument is considered to be the most reliable for the present study.

c. *Calculation of ambient relative humidity*

To calculate the relative humidity of the air, the saturation mixing ratio is required, in addition to the ambient vapor mixing ratio data from the hygrometer measurements. The saturation mixing ratio can be calculated using the ambient temperature measurements from the aircraft de-iced temperature probe. However the sensor on the temperature probe gets wet in liquid cloud, causing evaporative cooling that depresses the true reading by a few degrees (A. Woolley, FAAM, 2012, personal communication). This systematic error can create the illusion of unrealistically high relative humidities within liquid cloud layers. Instead, in water-saturated conditions we used measurements of the water vapor mixing ratio to derive the ambient temperature in the following manner. In the presence of liquid water, we assumed that the ambient vapor mixing ratio measurement represented the saturation mixing ratio. This was then converted to a saturation vapor pressure using the aircraft pressure measurement, from which the temperature was derived using the Clausius–Clapeyron equation. This technique was only used within liquid or mixed-phase conditions, where the assumption of water saturation was valid. In general, once out of liquid water the sensor on the temperature probe dries quickly and so in ice-only cloud or cloud-free regions, we used the aircraft measured temperature to calculate the relative humidity with respect to water and ice. The values for both the measured and derived temperature along the flight track are shown in Fig. 5b. The difference is most significant between 1410 and 1430 UTC (i.e., during run 10 when the aircraft spent considerable time in liquid cloud). The reader should note that heating rate calculations were performed using relative humidity data obtained from both the WVSS-II and the GE, and we found that in this case there was no significant dependence on the choice of hygrometer data used to perform the calculations.

5. Results of heating/cooling rate calculations

a. *Condensation*

Two flight legs had sufficient turbulence data to calculate heating rates associated with condensation growth of liquid droplets, specifically runs 10 and 13. Both runs occurred within regions of relatively high reflectivity associated with mesoscale precipitation structures.

We begin with run 10, as shown in Fig. 6. An RHI scan of reflectivity from CAMRa along the 253° radial is plotted in Fig. 6a, to illustrate the position of the aircraft within the frontal cloud system at the approximate time of the in situ measurements. During run 10 the ambient temperature was very close to the freezing level, where

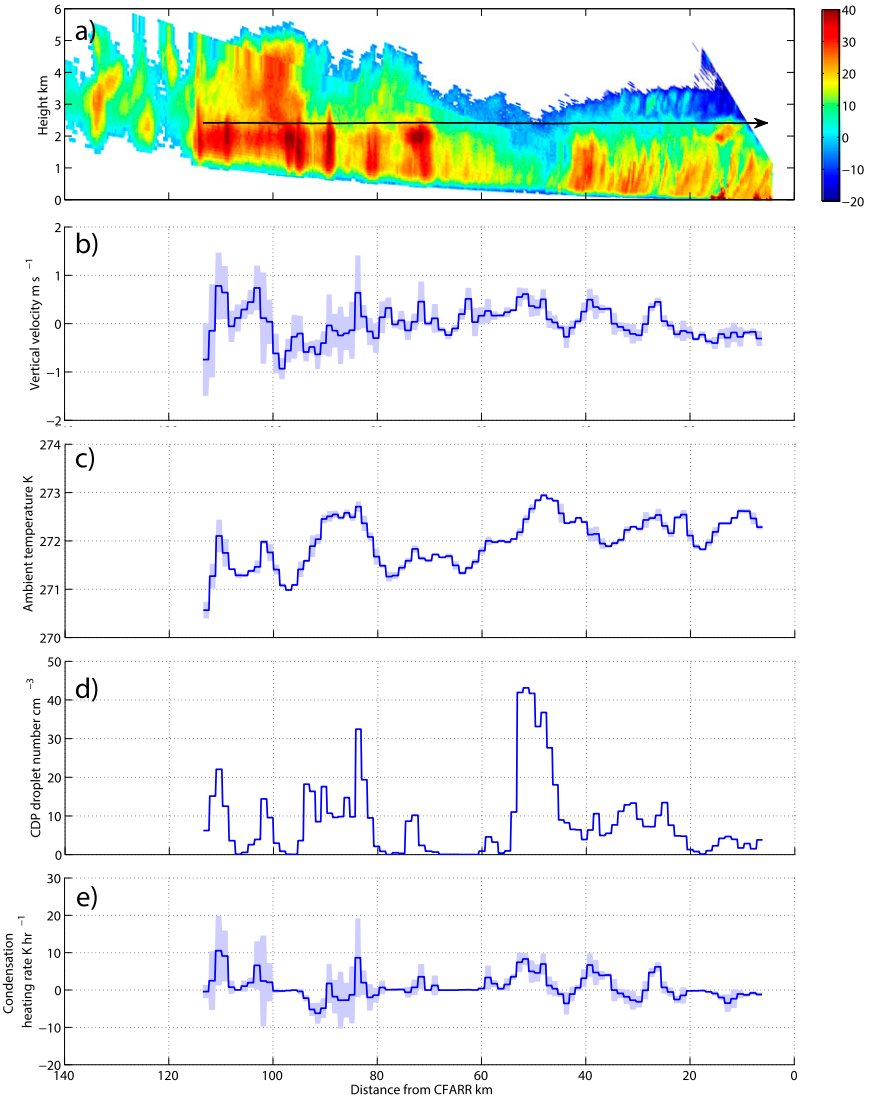

FIG. 6. Plots for run 10. (a) RHI scan of radar reflectivity (dBZ) from CAMRa at 1414 UTC, with black arrow illustrating the aircraft flight track; (b)–(d) plots of in situ data along the flight track showing vertical velocity, ambient temperature, and CDP droplet number concentration, respectively; and (e) condensation heating rate from the bin parcel model. The vertical velocity was produced by subtracting the mean vertical velocity value for the whole run from each 1-Hz measurement to correct for any systematic offset, following advice from FAAM scientists. In (b)–(e), the blue lines represent average values calculated over 1-km intervals from the 1-Hz data, while the shading represents the variability (±1 standard deviation).

liquid droplets dominated the number concentration, although larger solid particles were also detected during the run, details of which are discussed further in section 5d. The vertical velocity and temperature measurements are shown in Figs. 6b and 6c. The droplet number concentration and the heating rates due to condensation/evaporation along the flight track are shown in Figs. 6d and 6e, respectively. In Figs. 6b–e, we plot quantities as mean values calculated every eight data points (equivalent to a distance of approximately 1 km based on a constant airspeed of 120 m s^{-1}). The standard deviation over each 1-km distance is shown in light blue shading.[1] The mean vertical velocities lie within the range

[1] We recognize that variations in the 1-Hz turbulence data could be due to instrument noise as well as real variability in structure. However, because the degree of variation in the data along the flight track is not constant, which would be expected from instrument noise, we assume that the variations in vertical velocity are real.

$\pm 1\,m\,s^{-1}$; consequently, we compute maximum condensation heating rates of around $10\,K\,h^{-1}$ for run 10.

Figures 7a and 7b show an RHI scan from approximately an hour later (corresponding to run 13), by which time the system had begun to organize itself into a narrower, more intense rainband, consistent with the rainfall radar images in Fig. 2. During run 13, there were times when the turbulence probe was not working correctly because of icing problems associated with the previous run at cloud top. Hence, in Fig. 7c, data points are only shown where the turbulence probe was ice free and recording trustworthy data. Enough data remain to suggest that the aircraft passed through the convective feature at the leading edge of the front. Figure 7d shows that the droplet number concentrations were higher during run 13 compared to run 10, with a brief spike up to $120\,cm^{-3}$ coinciding with peak updrafts of $4 \pm 1.8\,m\,s^{-1}$. The CIP-100 probe also reveals some precipitation-sized particles during run 13, which appear to be associated with melting ice falling from above. Figure 7e reveals a maximum condensation heating rate of $56 \pm 25\,K\,h^{-1}$ for run 13. The standard deviation here is rather large, due to the variability in the vertical velocity. While we acknowledge that these calculations are based on limited turbulence probe data, our peak updraft value of $4 \pm 1.8\,m\,s^{-1}$ is not unreasonable when compared against previous observations of vertical velocities associated with cold frontal convection [e.g., $6.9\,m\,s^{-1}$ (Crosier et al. 2014) and $8\,m\,s^{-1}$ (Cox 1988)].

When running the bin parcel model to produce heating rates for condensation growth, we found that the model would spinup from the initial condition of water saturation to achieve a steady-state equilibrium supersaturation with respect to water, typically up to 0.5%. It was necessary to ensure that the model was allowed sufficient time to relax to this equilibrium state before the heating rates were calculated. For example, when the droplet number concentration was low (e.g., 10–$20\,cm^{-3}$; as frequently measured during run 10), the parcel model could take up to 100 s to equilibrate to some new quasi–steady state following initialization from water saturation. Mesoscale models typically use the method of saturation adjustment to handle condensation growth, whereby any excess water vapor above saturation that is left over at the end of the model time step is instantaneously assumed to condense onto existing liquid droplets. Previous work by Dearden et al. (2011) and Shipway and Hill (2012) have shown that in general, saturation adjustment is an excellent approximation relative to explicit treatments of droplet growth. However, in extreme cases, when vertical velocities are high enough and aerosol number concentrations low enough, the condensation relaxation time scale can be sufficiently long that the use of saturation adjustment becomes problematic (Lebo et al. 2012). For completeness we repeat our calculations of the condensation heating rates for runs 10 and 13 using a time-split saturation adjustment approach, where the new liquid water mass at the end of the 10-s model integration is solved by root finding such that the parcel is brought back to saturation. For the range of vertical velocities sampled, we found no significant difference between the results generated using saturation adjustment compared to those from the explicit method.

b. Deposition and sublimation

We now turn our attention to the solid phase, such that we may compare and contrast our findings to those derived in section 5a to ascertain the relative importance of ice phase processes for diabatic heating and cooling in this case. To begin with, we consider profile 11, which contained relatively high ice crystal number concentrations. Further, the ice crystal habit and the reduced levels of liquid water in this profile descent (less than $0.1\,g\,m^{-3}$) suggest that this was secondary ice that had formed initially via rime splintering, and was growing at the expense of liquid water due to the Bergeron–Findeisen process. Profile 13 exhibited very similar characteristics and indeed application of the parcel model to both profiles yielded similar results.

For simplicity, we begin by assuming that the shape of the ice crystals is spherical in both the bin and bulk schemes, such that the maximum dimension D as measured by the CIP probes is assumed to represent the diameter. We note that some schemes use an equivalent *volume* spherical diameter approach for vapor growth of ice (e.g., Reisner et al. 1998; Fridlind et al. 2007); however, we use the maximum dimension rather than an equivalent volume diameter because the volume of the ice crystals is not a quantity that we can measure directly, unlike dimension. Further, as noted in Westbrook et al. (2008), the rate of vapor growth of an ice particle is determined by its physical dimensions, not its volume. Westbrook et al. (2008) also show that spheres of the same maximum dimension provide an upper bound on the deposition heating rates from a nonspherical ice crystal, and thus the results from this section can be considered in the same way. We recognize that mass–size relationships are also an important consideration in numerical models, but for the purpose of calculating local rates of vapor growth of ice from the measured PSDs, knowledge of the ice mass is not required. However, we do consider the role of mass–size relationships later in section 5d, where we calculate cooling rates due to melting. We use ventilation coefficients given by Hall and Pruppacher (1976), and describe the variation of

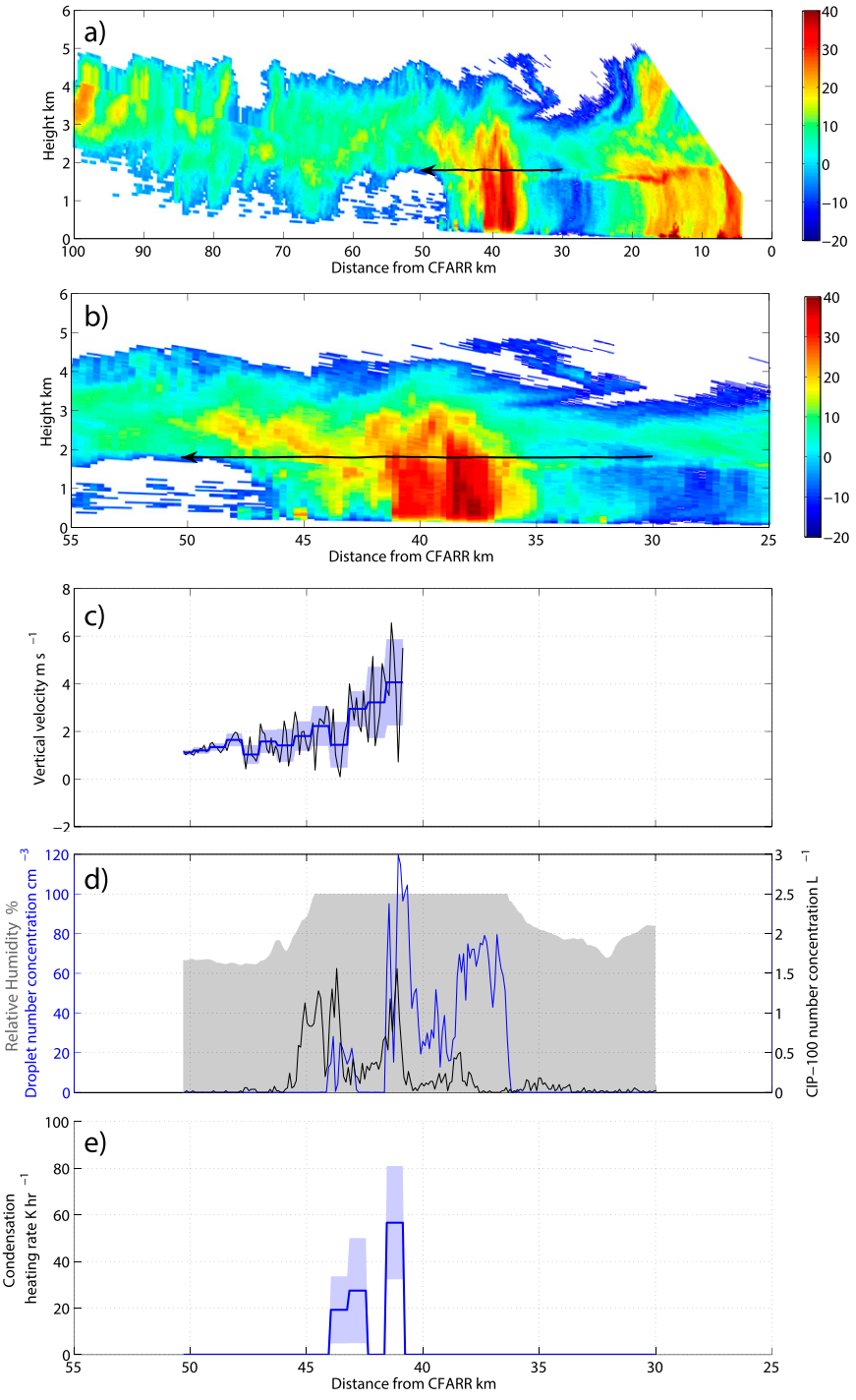

FIG. 7. Plots for run 13. (a) RHI scan of radar reflectivity (dBZ) from CAMRa at 1514 UTC; (b) close-up of the RHI scan, zoomed in on the area of interest; (c) in situ measurements along the flight track of vertical wind, with additional black line showing the 1-Hz data; (d) CDP droplet number concentration, CIP-100 number concentration for particles above 400 μm and relative humidity with respect to liquid, all at 1-Hz frequency; and (e) the condensation heating rate from the bin parcel model, showing the average values over 1-km intervals ± 1 standard deviation.

crystal fall speed with size using a power-law relationship appropriate for aggregates following LH74. In the case of the bulk model, negative exponential functions are fitted to the observed ice crystal size distributions. No reliable vertical velocity data were available during profile 11 due to problems associated with icing of the turbulence probe, thus we assume vertical velocities in the range $\pm 1\,\mathrm{m\,s^{-1}}$. However, the sensitivity of the deposition heating rates within this range of vertical velocity was found to be small.

Plots relating to profile 11 are shown in Fig. 8. The maximum deposition heating rates occur within the region where the number concentrations of ice are highest, producing a value of approximately $3\,\mathrm{K\,h^{-1}}$. We note that this is relatively small compared to the maximum heating rates from condensation growth ($56 \pm 25\,\mathrm{K\,h^{-1}}$ in run 13). Toward the end of the profile descent, the aircraft detected larger ice crystals at lower concentrations within subsaturated air, producing a diabatic cooling at a rate of typically $-1\,\mathrm{K\,h^{-1}}$. In both bin and bulk schemes the ventilation effect associated with the sedimentation of ice crystals accounts for approximately 50% of the diabatic effect, using the coefficients of Hall and Pruppacher. When comparing the magnitudes of the heating and cooling rates from the bin and bulk schemes (Figs. 8d and 8e), the agreement is generally good, although some small differences are still noticeable (e.g., when the aircraft was between 10 and 15 km from CFARR, where the bulk scheme overestimated the heating rates). This can be explained through considering the suitability of negative exponential fits used in the bulk scheme relative to the observed PSDs. Figure 9a shows a comparison of the time mean PSD observed during profile 11 with a total number-conserving negative exponential fit. The PSDs are expressed in the form dN/dD [i.e., the number concentration $N(D)$ normalized with respect to the width of the size bins, dD]. There is a tendency for the exponential fit to underestimate the number concentration of ice crystals at sizes $D > 3$ mm, while slightly overestimating concentrations between 200 μm and 2 mm. This discrepancy is slightly more noticeable in Fig. 9b, which plots the quantity DdN/dD. The integral $\int_{D_{\min}}^{\infty} DN(D)\,dD$ (i.e., the first moment of the distribution) is a useful quantity as it is proportional to the growth rate of the ice crystals from the vapor phase within the size range $D_{\min}$ to infinity. Figure 9c evaluates this integral for the measured and fitted size distributions as a function of $D_{\min}$; any differences in the heating/cooling rates between the bin and bulk schemes can be understood in terms of this quantity. Figure 9c shows that in both schemes, the rate of change of ice mass is dominated by crystals below 2 mm in size, and that the underestimation of ice crystals at larger sizes (>3 mm) in the bulk scheme has very little impact, and hence makes little difference to the overall growth rate of the ice crystals. However, the occasionally higher heating and cooling rates in the bulk scheme can be explained in terms of the slight tendency to overestimate ice crystal concentrations below 2 mm.

The parcel model was also used to calculate sublimation cooling rates during run 15 (i.e., within the cloud layer trailing the leading edge of the front). Although this run was within the temperature regime required for rime splintering to occur, columnar ice crystals indicative of secondary ice production were largely absent. This is because the relative humidity along this section was below both ice and water saturation, and so in the absence of any liquid water, active rime splintering was not possible. The microphysics measurements suggest that the ice detected during run 15 had formed via primary nucleation in the saturated layer above, with the ice crystals then sedimenting into the subsaturated air along the flight track. The resulting sublimation cooling rates for both bin and bulk microphysics schemes are shown in Figs. 10d and 10e, again assuming spherical ice. The effects of ventilation are even stronger in run 15 compared to profile 11; this is because although there are fewer ice crystals, they are generally bigger in size and thus have a greater fall speed. The bulk cooling rates generally agree well with those from the bin scheme, although again a slight tendency to overestimate the cooling rates is noted at certain times during the run. The impact of fitting negative exponentials was also considered for the data collected during run 15 and is shown in Fig. 11. The fit is shown to be appropriate across most size ranges, with only a slight overestimation of number concentrations at smaller sizes, which leads to a slightly larger value of $\int DN(D)\,dD$ when integrated from 0 to ∞.

THE EFFECTS OF ICE CRYSTAL HABIT

In producing Figs. 8d,e and 10d,e, the ice crystals were modeled as simple spheres with a diameter equal to the maximum dimension D as measured by the CIP probes. However, images from the 2D-S probe during profile 11 clearly showed pristine columns and needles; similarly run 15 showed large snow aggregates made up of planar crystals, with pristine stellar ice crystals present up to around 600 μm (see Figs. 12a and 12b). Ice crystal geometry is known to be a key factor in determining rates of crystal growth. For instance, the theoretical modeling study of Sulia and Harrington (2011) found that the ability to account for changes in the aspect ratio of spheroidal ice crystals is most important at temperature regimes where pronounced habits exist ($-15°$ and $-6°$C), and at ice number concentrations between 1 and $100\,\mathrm{L^{-1}}$; we note that both these criteria apply here.

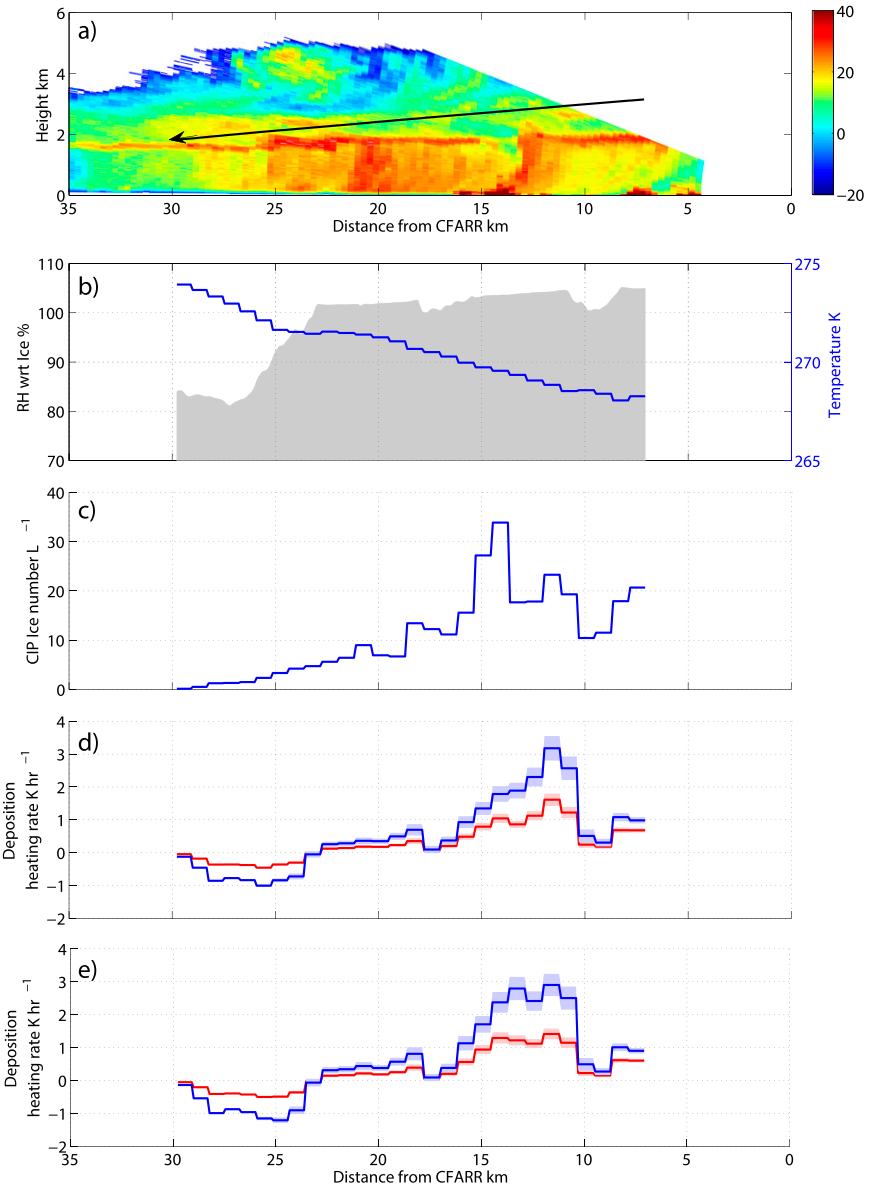

FIG. 8. Plots for profile 11. (a) RHI scan of radar reflectivity from CAMRa at 1510 UTC, focusing on the flight track region; (b) in situ measurements along the flight track of ambient temperature, with relative humidity with respect to ice in gray shading; (c) ice crystal number concentration; (d),(e) deposition heating rate from the bin and bulk parcel models assuming spherical ice. In (d),(e), the blue lines account for the effect of ventilation due to sedimentation, while the red line assumes the ice crystals have negligible fall speed with respect to the air parcel (i.e., no ventilation).

Furthermore, other modeling approaches based on capacitance theory have led to advances in the treatment of crystal growth rates for realistic crystal shapes, including aggregates (e.g., Westbrook et al. 2008).

Figures 13a and 13b show estimates of the instantaneous diabatic heating and cooling rates along profile 11 and run 15, respectively, taking into account the shape of the ice crystals in the equations used to represent diffusion growth and the effects of ventilation (see the appendix for further details). In both cases, when ventilation effects are ignored the 1-km average heating/cooling rates along the flight track are reduced by a factor of approximately 2 with respect to those shown in Figs. 8 and 10, although the standard deviation increases due to the variability in the range of crystal shapes encountered. When ventilation effects are included, the magnitudes of

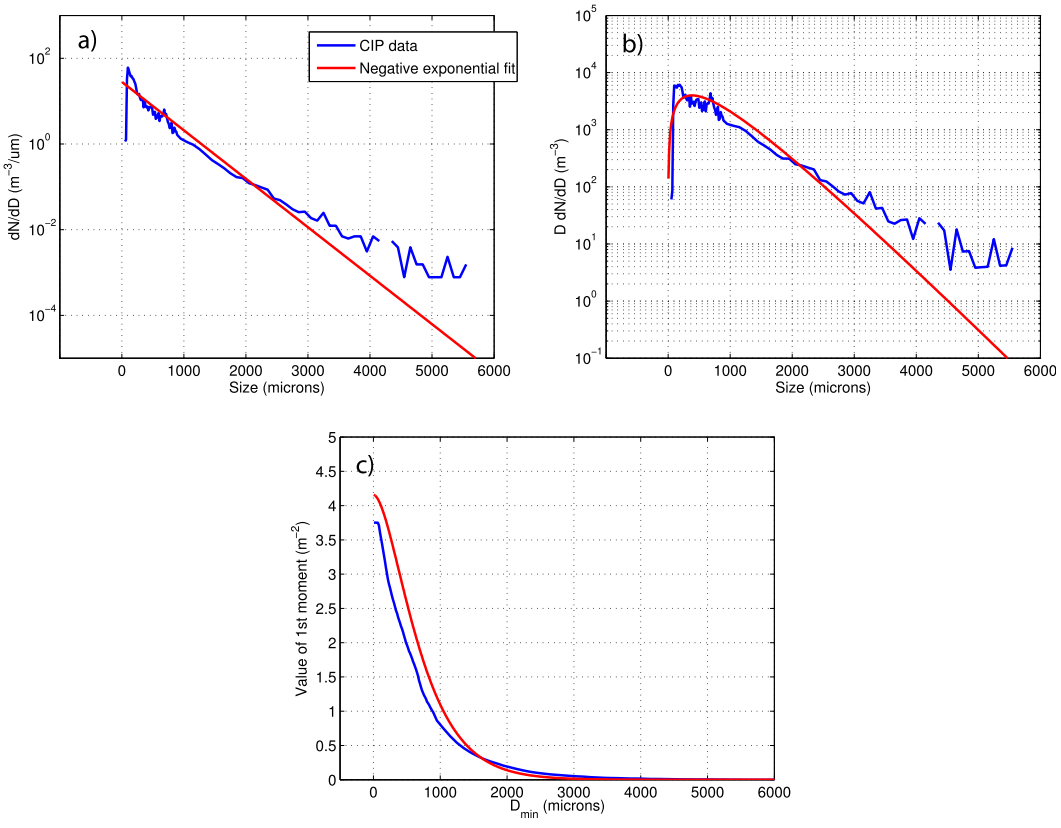

FIG. 9. Analysis of the time mean ice particle size distribution for profile 11 (1511–1515 UTC). Observations (from the merged CIP data) are shown in blue; negative exponential fit in red. (a) Comparison of dN/dD, (b) comparison of DdN/dD, and (c) comparison of $\int_{D_{min}}^{\infty} DN(D)\,dD$ evaluated as a function of D_{min}. The latter represents the contribution of particles with size $\geq D_{min}$ to the overall growth/evaporation rate by vapor diffusion.

the heating/cooling rates increase as before, but to a lesser degree than in Figs. 8 and 10. This shows that the subtleties of crystal habit are also important in determining the extent to which ventilation enhances the rate of change of ice crystal mass via vapor diffusion.

c. *Riming*

Here we calculate rates of latent heat release associated with the growth of falling ice crystals by collection of cloud droplets (riming). We concentrate our analysis on run 14, just below cloud top as shown in Fig. 14a, where sufficient amounts of liquid water were present and the high-resolution images from the 2D-S probe reveal planar ice crystals exhibiting evidence of rime growth. Because of the size of the ice crystals imaged in run 14, we use data from the CIP-100 probe to initialize the parcel model.

Ice crystal concentrations were low initially (Figs. 14b–d), transitioning toward an ice-free regime characterized by large supercooled drops, presumably formed by collision–coalescence of liquid droplets, which were present for most of the run. The heating rates for both riming and deposition are also shown in Fig. 14e, calculated with the bulk parcel model using the liquid-ice collection parameterization described in Morrison et al. (2005). Here we see that the heating rates directly associated with riming are approximately an order of magnitude less than for deposition heating, despite the comparable mass growth rates for each mechanism. This is because of the smaller latent heat coefficient of fusion compared to the latent heat of sublimation. 2D-S images of the columnar ice crystals from profiles 11 and 13 reveal little evidence of significant growth due to riming, presumably because the Bergeron–Findeisen process had already removed much of the liquid in response to the production of secondary ice splinters. Thus, we note the importance of riming in this case in terms of the initiation of the rime splintering process, but once the secondary ice is produced, deposition and aggregation become the major growth mechanisms, limiting the overall impact of riming as a source of diabatic heating. Although we only show riming rates from the bulk microphysics, given that the heating rates from riming are so small in this case, any discrepancies relating to the use

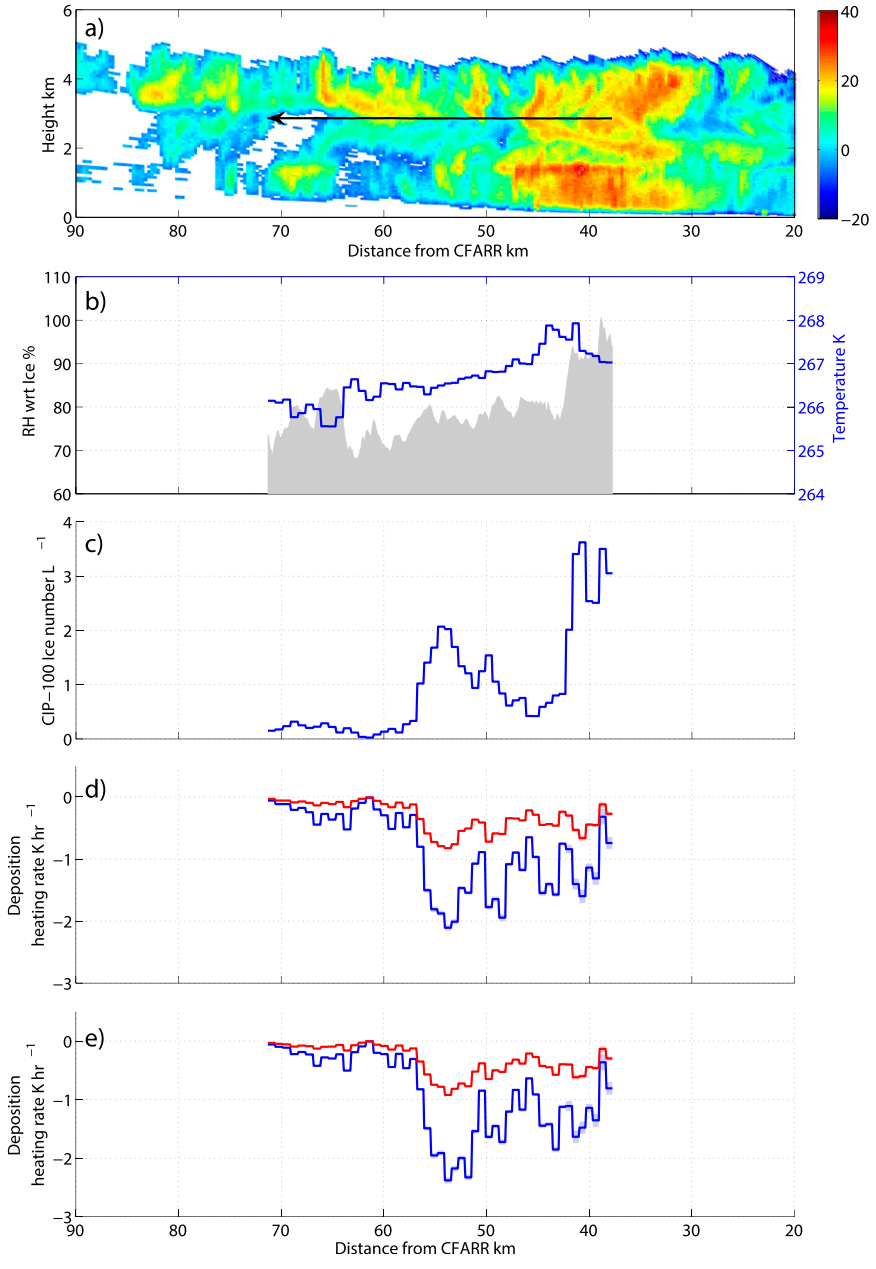

FIG. 10. As in Fig. 8, but for run 15. The RHI scan shown in (a) was taken at 1547 UTC.

of gamma and negative exponential functions in this context are unlikely to have any significant impacts.

d. Melting

Cooling rates associated with melting of falling ice crystals are calculated for run 10, where the aircraft flew along a straight and level trajectory close enough to the top of the melting layer to warrant such a calculation. The in situ data, in conjunction with the RHI scans from CAMRa (Figs. 6a and 15a), suggest that melting ice makes a significant contribution to the intensity of precipitation. For instance, ice was only detected during the first half or so of run 10 (Fig. 15b), during a time when the RHI scans revealed the highest reflectivity values and the coldest cloud tops. Images from the cloud probes reveal that these ice crystals consisted mainly of rimed snow and column aggregates, supporting the idea that this ice had formed higher up in the cloud and was falling down to the flight level. No ice was detected along the flight track of run 10 within 50 km or so of CFARR (except very briefly toward the end of the run), and within this range the RHI scans show generally warmer cloud tops,

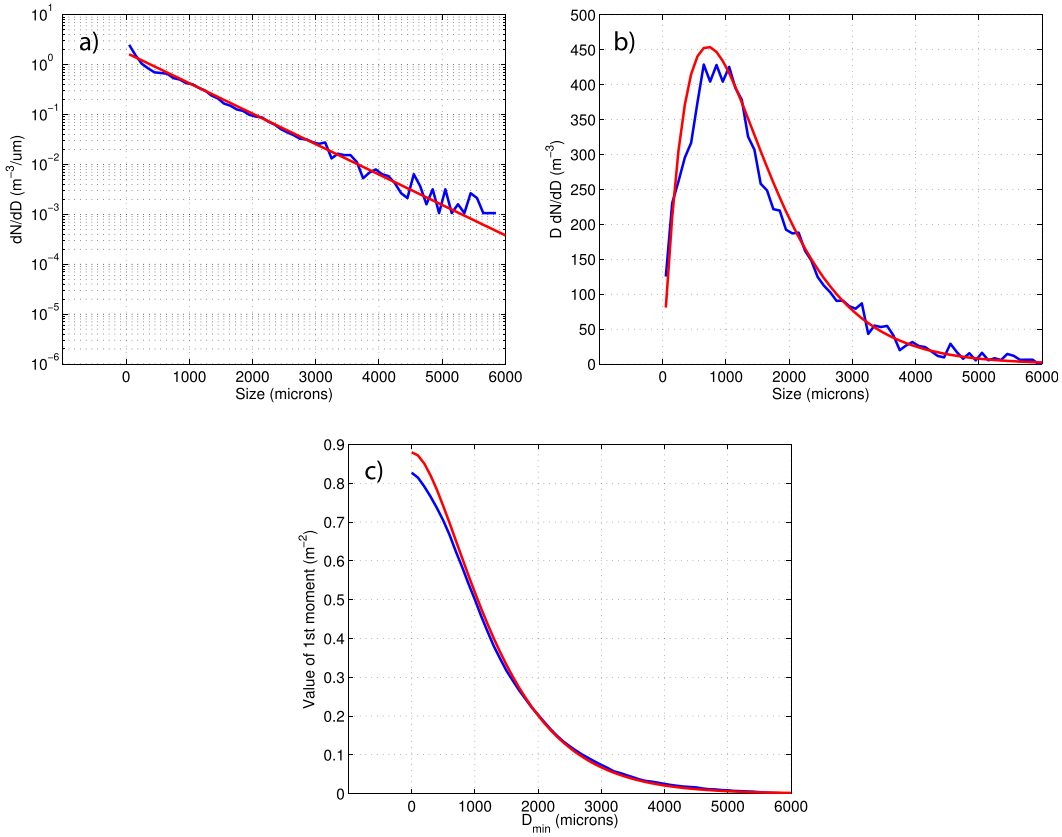

FIG. 11. As in Fig. 9, but for the time mean ice PSD for run 15 (1549–1557 UTC).

weaker reflectivity values, and no evidence of a melting bright band. This suggests that at this particular time, the precipitation within the first 50 km of CFARR originated via collision–coalescence of liquid drops, whereas the higher reflectivity values farther west were associated with the sedimentation and melting of large ice crystals.

To calculate the mean cooling rates associated with the melting process over a given depth Δz, the in situ microphysics measurements are used to quantify the flux of ice falling through the top of the melting layer. For a given ice PSD, the melting rate (kg kg^{-1} s^{-1}) in a given size bin i is calculated as

$$\left.\frac{dq_i}{dt}\right|_{\text{mlt}} = \frac{q_i V_i}{\Delta z}. \tag{3}$$

In Eq. (3), q_i is the ice mass mixing ratio and V_i refers to the fall speed of the ice crystals following LH74 (see the appendix). The depth of the melting layer Δz is estimated from the RHI scan of differential reflectivity (Fig. 15a), which we place between 300 and 500 m. Integrating Eq. (3) over the range of relevant sizes gives the bulk melting rate. Equation (3) implicitly assumes that aggregation of ice crystals does not occur within the melting layer. While aggregation of melting snow would not affect the mass mixing ratio, it would change the number of crystals as a function of size, tending toward an increase in the number of larger particles and a decrease in the number of smaller particles. This would lead to an overall increase in the mean particle fall speed and therefore potentially impact the melting rates. Unfortunately we do not have any in situ measurements at the bottom of the melting layer to quantify the extent to which the particle size distribution is affected by aggregation, but we note that previous studies (e.g., Braun and Houze 1995) have found very good agreement between cooling rates determined at the top and bottom of the melting layer, suggesting that collection processes within the melting layer do not significantly affect the cooling rate.

To capture those ice crystals large enough to have fallen from above under gravitational settling, we use data from the CIP-100 probe, assuming a power-law relationship between the mass of a crystal m and its size D, of the form $m = c_s D^{d_s}$. We confine ourselves to the use of CIP-100 data above 400 μm to evaluate the melting rates, since drizzle drops were also detected during this run, but the processing software often mistook these for ice. While this has the potential to reject

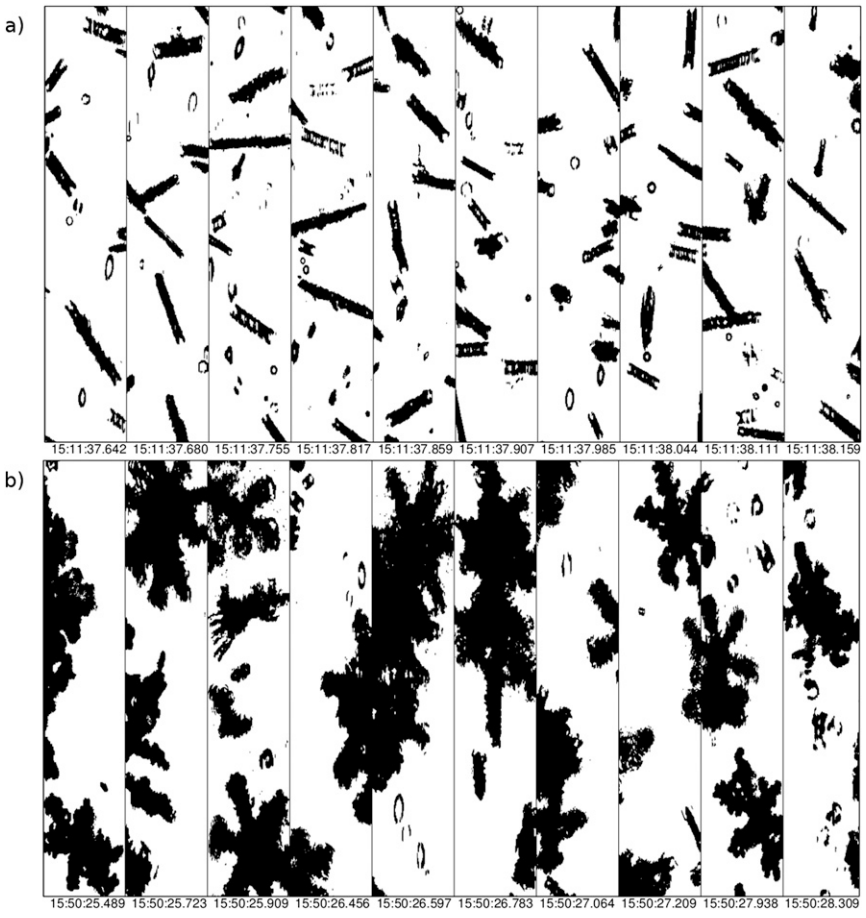

FIG. 12. Images of ice crystals from the 2D-S probe during (a) profile 11 at 1511 UTC, near the start of the profile descent and (b) run 15 at 1550 UTC, near the start of the run.

some real ice crystals, our calculations show that ignoring the smaller cloud particles does not have a significant impact on the ice mass flux. The results of the cooling rate calculations associated with melting ice in run 10 are shown in Fig. 15. Three separate cooling rate calculations are performed, each using different values for c_s and d_s in the mass–size relationship. Figure 15c uses coefficients $c_s = 0.037$ and $d_s = 1.9$ (for size D in millimeters) as given in LH74; Fig. 15d uses $c_s = 0.069$ and $d_s = 2.0$, as in the Met Office microphysics scheme of WB99; and Fig. 15e uses coefficients appropriate for ice spheres, such that $c_s = \pi\rho_i/6$ (with $\rho_i = 100\,\mathrm{kg\,m^{-3}}$) and $d_s = 3.0$. We refer to the latter case as RH84, since it was used in the frontal rainband modeling studies of Rutledge and Hobbs (1983, 1984) although it is still employed in more recent schemes as well (e.g., Morrison et al. 2005), which is commonly used in the Weather Research and Forecasting Model (Skamarock et al. 2008). The results show that the choice of mass–size relationship has a significant impact on the magnitude of the cooling associated with melting ice. For snow aggregates, the exponent d_s is believed to be close to 2.0 (Westbrook et al. 2004), in which case the RH84 coefficients applied to the measured PSDs would overestimate the ice mass, and hence the melting rate, considerably. Cooling rates due to melting in NCFRs have also been derived by Marécal et al. (1993), using a microphysical retrieval model constrained by wind fields obtained from dual-Doppler radar observations. A comparison reveals that our peak cooling rates are approximately an order of magnitude smaller than those in Marécal et al.; this is most likely because of the lack of graupel particles in the present case study.

6. Discussion

Having attempted to quantify rates of latent heating and cooling from the available in situ data, we now consider the possible implications in terms of potential vorticity generation, and how this may influence the dynamic evolution of the frontal system. It would certainly appear that the dominant mechanism governing the mesoscale evolution of this particular cold front is

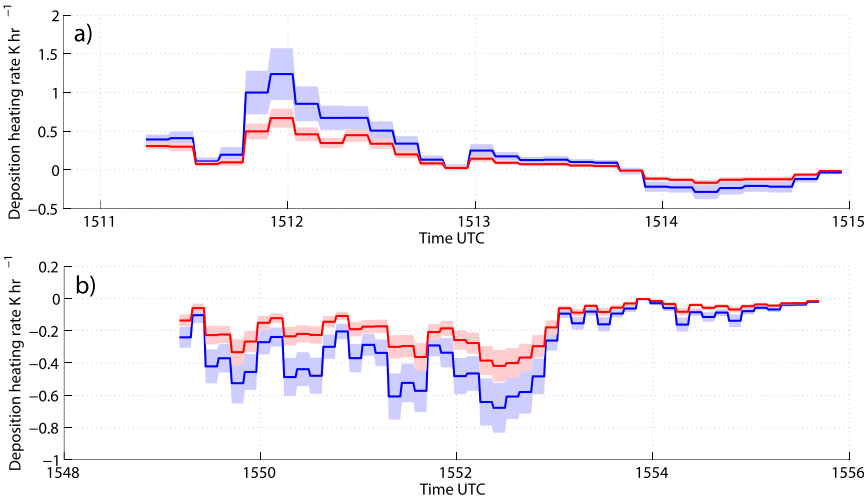

FIG. 13. Deposition heating and sublimation cooling rates, plotted as time series, from the bin parcel model for (a) profile 11 and (b) run 15, accounting for the effects of ice crystal shape as described in the appendix. As in Figs. 8 and 10, the red line represents calculations performed without the effects of ventilation, and the blue line represents calculations performed with ventilation.

the transition from ana to kata type, which is controlled by the synoptic-scale dynamics. Thus, the question that arises is what role does the cloud microphysics play in modifying the precipitation structure associated with the front within the context of this large-scale forcing? Clearly the largest diabatic term we derive here comes from condensation growth within the updrafts at the leading edge of the advancing cold sector air. Because such heating takes place in a region where the absolute vorticity is likely to be high because of the cyclonic circulation at the frontal boundary, one would expect localized generation of positive potential vorticity below the level of maximum condensation heating. It is conceivable that such positive PV anomalies would act to enhance the low-level curvature vorticity around the front, producing stronger convection and a more intense low-level jet, as in the case of Lackmann (2002). The convective updrafts are also responsible for the transportation of condensate to altitudes where subsequent growth processes can lead to additional diabatic effects. A consideration of the implications of latent heat release and uptake via the solid phase is complicated by the fact that ice is often initiated in one place (e.g., by heterogeneous nucleation) and is then subsequently advected to another region of the cloud system. The impact of heating associated with deposition growth of ice columns may be reduced in the present case since ice columns were detected in the prefrontal warm sector air, where the absolute vorticity is likely to be weak and thus any diabatic modification of the PV field would be smaller than if it took place within the updrafts at the leading edge of the front. The diabatic influence of melting ice may be more significant, however, because it is concentrated within a relatively shallow layer a few hundred meters thick. Indeed previous studies have noted the role of melting in the generation of mesoscale circulations and the maintenance and initiation of mesoscale downdrafts (e.g., Szeto et al. 1988a,b).

It is also interesting that the across-front RHI scans from CAMRa reveal some evidence of a trailing stratiform cloud layer, behind the leading edge of the front (e.g., Fig. 7a). While the concept of rearward-sloping ascent is a phenomenon typically associated with ana fronts, it has been noted before in the context of kata fronts Browning (1995, their Fig. 7). However, unlike the case described by Browning, this front-to-rear airflow in the present case study appears to be saturated, with precipitation-sized ice crystals falling from it. We note the absence of any significant precipitation behind the NCFR in the Met Office rainfall radar maps shown in Fig. 2; indeed, we have shown evidence of ice crystal sublimation in the cloud layer behind the leading edge of the front. However, the latent cooling effect would act to modify the temperature profile below cloud base, potentially impacting on the strength of the downdrafts and the intensity of the line convection, in accordance with a simple density current model. Browning also comments that the wind shear at the interface between the warm and advancing cold air masses has the potential to set up Kelvin–Helmholtz waves, which upon breaking could result in turbulent surges that perturb the propagation speed of the front. Braided patterns in the Doppler radar data, specifically in the vertical gradient of Doppler

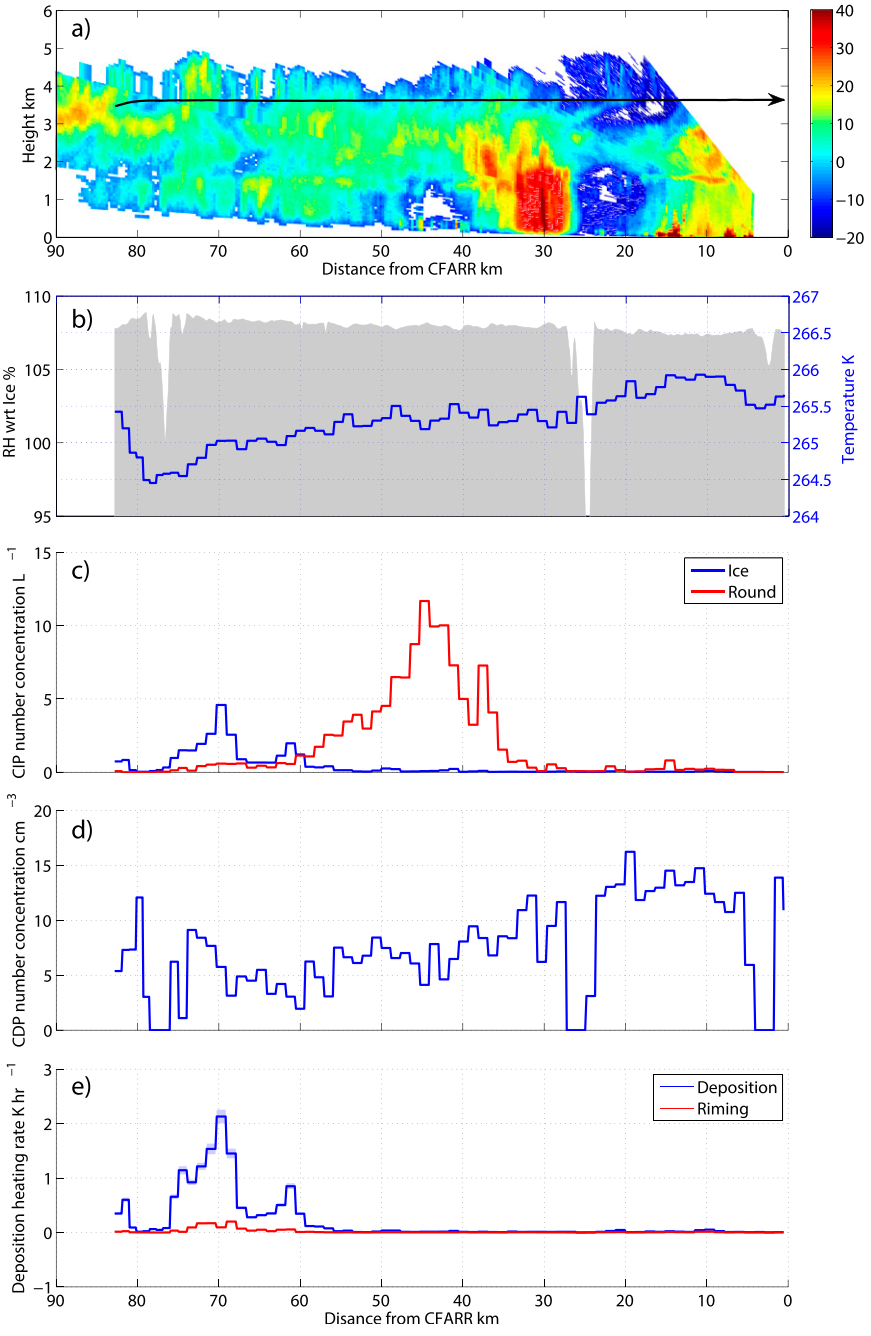

FIG. 14. Plots for run 14. (a) RHI scan of radar reflectivity from CAMRa at 1520 UTC, (b) in situ measurements along the flight track of ambient temperature and relative humidity with respect to ice, (c) number concentrations of ice (blue) and drizzle (red) from the CIP-100, (d) CDP droplet number concentration, and (e) heating rates for deposition (blue) and riming (red) as derived from the bulk parcel model.

velocity, are indicative of Kelvin–Helmholtz billows (e.g., Chapman and Browning 1998). While there was no clear evidence of such braided patterns in the CAMRa data for this case study, we did at least observe that the radar measurements of spectral width were much higher within the trailing stratiform region of the cloud, which is consistent with enhanced turbulence caused by wind shear at the interface of the warm and cold air masses. While such fluid dynamic effects are not the subject of this paper, we note its potential

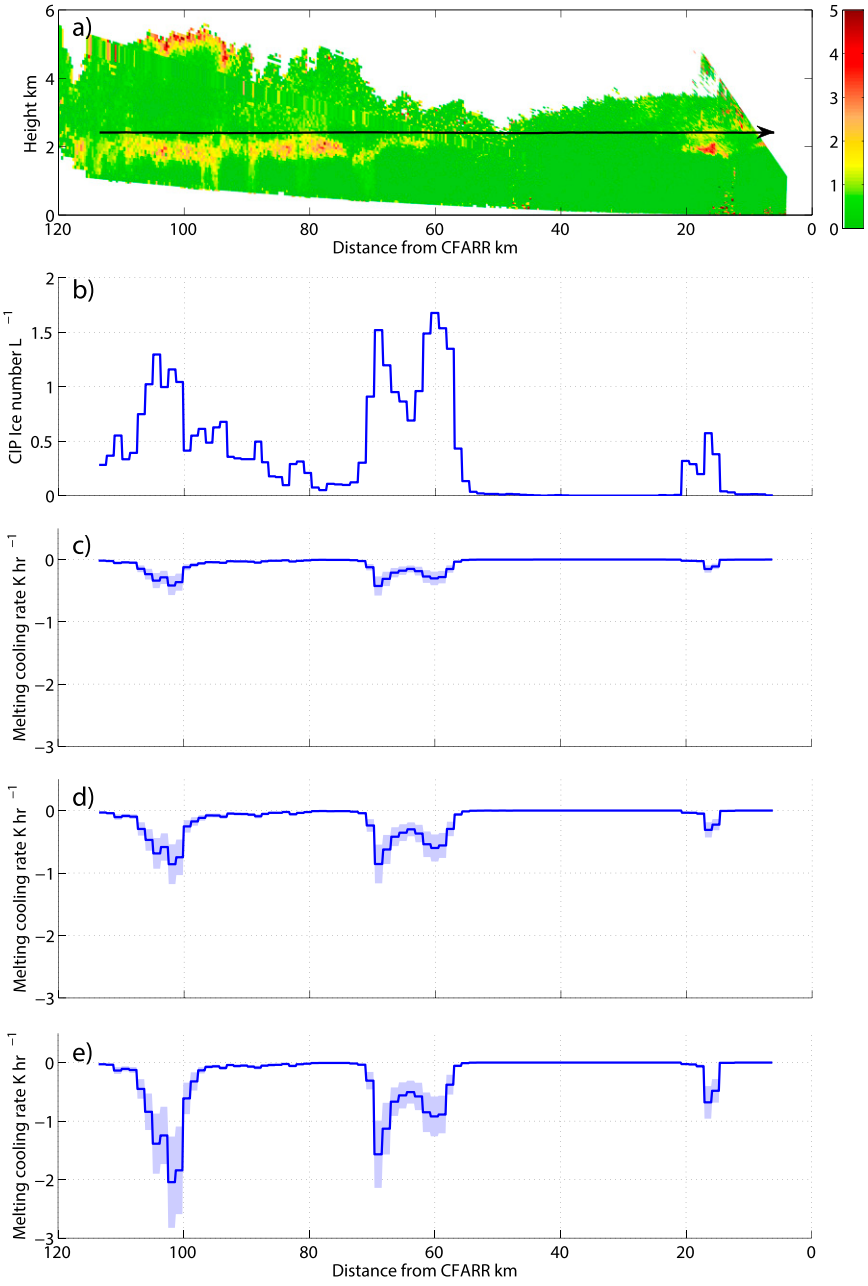

FIG. 15. Additional plots for run 10. (a) RHI scan of differential reflectivity from CAMRa at 1414 UTC, (b) in situ measurements along the flight track of ice number concentration above 400 μm from the CIP-100 probe, and cooling rates associated with the melting of ice, using mass-size relationships as follows: (c) LH74, (d) WB99, and (e) RH84.

importance as a mechanism for influencing the strength of the cold air inflow at low levels.

The other main consideration of this paper was the use of the parcel model framework to identify potential weaknesses associated with microphysics parameterizations that are typically used in current operational forecast models. In terms of representing condensation growth in numerical models, we found the method of saturation adjustment to be valid for the range of vertical velocities that we were able to measure in this case study. However, the method is reliant on the ability of models to adequately represent the subgrid variability in the vertical velocity field, something that remains a challenge for forecast models at current operational resolutions (e.g., Tonttila et al. 2011). Because of the strong sensitivity of the condensation heating rate to the

magnitude of the vertical wind, there is potential for error in forecast models if the subgrid-scale vertical velocities are not adequately parameterized, thus leading to a misrepresentation of the feedbacks involved between the microphysics and dynamics in the simulation. With regards to the ice phase, the assumption of spherical crystals was found to be too simplistic as many of the crystals imaged by the cloud probes had distinctly nonspherical habits. Indeed, despite the relatively shallow depth of the frontal cloud, we noticed a strong contrast between the pristine plates and stellar ice crystals at or close to cloud top, and the long columns that dominated elsewhere. Representing these ice crystals as spheres with diameters equal to their maximum dimension led to overestimation of the instantaneous heating and cooling rates by a factor of approximately 2 in the case of vapor diffusion. In the case of melting, the assumption of ice spheres produced even larger discrepancies due to overestimation of ice particle mass, and this places emphasis on the importance of using appropriate mass–size relationships in models. A slight issue was also found concerning the use of negative exponential fits relative to the observed ice PSDs, as the fits tended to overestimate number concentrations at smaller sizes and underestimate the concentrations at the largest sizes. The impact of these discrepancies leads to a slight overestimation of the local heating/cooling rates relative to the observed PSDs. We note that in bulk schemes that predict only a single moment of the ice distribution (those typically used in operational models), the intercept parameter of the negative exponential is often diagnosed simply as a function of temperature (e.g., Hong et al. 2004); in such cases, the discrepancies with respect to the observed PSDs may be even larger.

Our results also show that the ventilation of sedimenting ice particles has an important effect on the local diabatic heating/cooling rates, and that the magnitude is dependent on crystal habit. Recently, new treatments of ice vapor growth based on an adaptive treatment of crystal habit have emerged (e.g., Harrington et al. 2013a,b; Sulia et al. 2013), where ice crystals are represented as spheroids with an aspect ratio that is allowed to evolve as a function of temperature. Such schemes are ideally suited to modeling the vapor growth of relatively simple habits like columns and plates, as opposed to more complex polycrystals and aggregates. Traditionally, the autoconversion threshold has been a key parameter in bulk schemes, as it controls the transfer of solid mass between multiple subclasses [e.g., from the cloud ice category (representative of smaller pristine crystals) to the snow category, which can include larger pristine crystals as well as aggregates]. Unfortunately, as noted in Morrison et al. (2008), the size threshold for autoconversion is a poorly constrained parameter that is often treated somewhat arbitrarily. We argue that the validity of such thresholds becomes even more tenuous when used in conjunction with adaptive habit schemes. For example, the preferential growth of spheroids along the axis of maximum dimension means that, all else being equal, their size would evolve much quicker than that of an isometric crystal of the same volume, and in such cases the use of a fixed autoconversion threshold could unrealistically accelerate the onset of snow. Thus, when implementing parameterizations of adaptive growth in bulk schemes, it may be necessary to replace the snow category with an aggregates category, such that the transfer of ice mass is handled via an appropriate parameterization of the ice collection process.

7. Summary and conclusions

In this paper we have quantified instantaneous rates of heating and cooling for liquid and ice phase processes associated with a narrow cold frontal rainband using a combination of in situ measurements and a Lagrangian parcel model framework. We have focused specifically on in situ measurements taken during the final stages of the frontal transition from ana to kata type, where the data were most robust. We have shown that the diabatic terms of largest magnitude are associated with the liquid phase (i.e., from condensation and evaporation), in line with previous idealized modeling studies. The diabatic effects of ice phase processes (deposition/sublimation and melting) were found to be at least an order of magnitude smaller than the peak heating rates from condensation, although they tend to cover a wide horizontal extent, and in the case of melting, concentrated within a shallow layer. Ice growth rates by riming were found to be an order of magnitude smaller still, and therefore do not appear to be high enough to result in a significant diabatic effect in this particular case study. Precipitating ice is shown to produce a cooling effect via sublimation and melting, which could influence the mesoscale evolution of the front by modifying the temperature profile below cloud base. Based on this case study, we conclude that in terms of PV generation, the role of the ice phase is most likely to be important during the ana phase of the front, where sublimation and melting can directly influence the strength of the cold air inflow. Then as the system matures and the front transitions from ana to kata, the diabatic influence of the ice phase is reduced as a consequence of the dry intrusion aloft, which pushes the ice into the warm sector ahead of the cold front. Therefore, the strong dynamical forcing of this wintertime kata cold front would appear to

control the extent to which ice phase processes contribute diabatically to the mesoscale evolution. Further study of other wintertime cold front cases is necessary to establish the generality of this result.

We have also attempted to validate the performance of a typical bulk microphysics scheme in terms of its representation of diabatic heating and cooling, using a detailed bin-resolved scheme and the in situ observations as a benchmark. Our main conclusions from this comparison are listed below:

- For the conditions encountered in this study, the method of saturation adjustment used to represent condensation growth in bulk schemes was found to be an excellent approximation compared to explicit treatments.
- Bulk schemes that treat ice crystals as simple spheres are shown to be inadequate in terms of simulating local rates of diabatic heating and cooling associated with changes in ice crystal mass, particularly via vapor diffusion and melting. This calls for bulk schemes to be able to account for variations in ice crystal shape in order to simulate more realistic diabatic heating and cooling profiles.
- Ventilation effects were found to influence the magnitude of the local diabatic heating and cooling rates by as much as a factor of 2 or more. However, we did note that ventilation coefficients were not quite as strong when the effects of ice crystal habit were accounted for. Bulk schemes that do not include the effects of crystal habit, therefore, have the potential to misrepresent the effects of ventilation;
- In terms of their diabatic effect, the use of negative exponential fits to describe the form of ice PSDs in the bulk scheme was generally found to be a reasonably good approximation to the observed PSDs. We did note a slight tendency to overestimate number concentrations between 200 μm and 2 mm approximately, which was within a size range that was found to be important in determining the growth rate (and hence heating/cooling rate) of ice crystals via the vapor phase. Discrepancies at larger sizes (>3 mm) were found to have a much smaller impact on the instantaneous diabatic heating/cooling rates, although we note the potential for such errors to affect aggregation and riming rates, which may lead to more significant differences over longer time scales.

Given that our conclusions are obtained through consideration of a single case study, it would be useful to reproduce this analysis for a larger sample of midlatitude weather systems, to help put these results into context. In reaching these conclusions, it must also be remembered that we initialize our parcel model from the in situ measurements. In doing so, we bypass many of the uncertainties surrounding the parameterization of droplet activation and ice nucleation in cloud microphysics schemes. We also acknowledge the potential for bulk microphysical prognostic variables (mass mixing ratio and number concentration) to be influenced by other poorly constrained parameters, such as autoconversion thresholds and the assumed collection efficiencies for aggregation and riming, which could lead to additional errors in terms of diabatic effects. We recommend that a useful way forward would be to perform a series of mesoscale model experiments designed to explore the sensitivity of this case, and others, to the representation of ice phase microphysics, particularly to ascertain the extent to which the simulated mesoscale features are sensitive to those aspects of a typical bulk microphysics scheme that we have identified here, and thus whether the additional complexity in terms of the ice phase microphysics can be justified.

Acknowledgments. This work was funded by the Natural Environment Research Council (NERC) as part of the Storm Risk Mitigation Programme (NE/I005234/1), in partnership with the Met Office. We acknowledge the Facility of Airborne Atmospheric Measurements for contributing the core aircraft data; we also acknowledge the Chilbolton Facility for Atmospheric and Radio Research for providing the Doppler radar data.

APPENDIX

Parcel Model Equations

a. Growth of liquid droplets by vapor diffusion

The rate of change of mass ($\mathrm{kg\,s^{-1}}$) of a spherical liquid droplet of a given diameter D due to condensation/evaporation is given by

$$\left.\frac{dm(D)}{dt}\right|_{\mathrm{con}} = \frac{2\pi D s_{\mathrm{liq}}}{AB_{\mathrm{liq}}}, \tag{A1}$$

where s_{liq} is the supersaturation with respect to liquid, equal to $(e/e_{\mathrm{liq}}) - 1$, where e is the water vapor pressure and e_{liq} is the saturation vapor pressure over liquid, and

$$AB_{\mathrm{liq}} = \left[\frac{R_v T}{e_{\mathrm{liq}} D_V^*} + \frac{L_v}{TK_T^*}\left(\frac{L_v}{TR_v} - 1\right)\right], \tag{A2}$$

where R_v is the gas constant for water vapor, D_V^* is the modified diffusivity of air, L_v is the latent heat of vaporization, T is temperature, and K_T^* is the modified thermal conductivity of air. In Eq. (A1), no ventilation

effects are considered for cloud droplets. The overall rate of change of liquid mass, PRC (kg kg^{-1} s^{-1}), due to condensation/evaporation is then computed as

$$\mathrm{PRC} = \int_0^\infty N_D(D) \left.\frac{dm(D)}{dt}\right|_{\mathrm{con}} dD, \tag{A3}$$

where $N_D(D)$ is the droplet number concentration. Converting integrals to summations in the bin parcel model, using data from the CDP probe, this becomes

$$\mathrm{PRC} = \sum_{D=0}^{50\,\mu\mathrm{m}} N_D(D) \left.\frac{dm(D)}{dt}\right|_{\mathrm{con}}. \tag{A4}$$

In the bulk scheme, gamma functions are fitted to the measured cloud droplet size distributions: $N(D) = D^{\alpha_d} N_{0\mathrm{d}} \exp(-\lambda_d D)$, where α_d is the shape parameter, $N_{0\mathrm{d}}$ is the intercept parameter, and λ_d is the slope parameter. Consequently, following Eq. (A3), PRC in the bulk scheme is calculated as

$$\begin{aligned}\mathrm{PRC} &= \frac{2\pi N_{0\mathrm{d}} s_{\mathrm{liq}}}{AB_{\mathrm{liq}}} \int_0^\infty D^{\alpha_d} \exp(-\lambda_d D)\, dD \\ &= \frac{2\pi N_{0\mathrm{d}} s_{\mathrm{liq}}}{AB_{\mathrm{liq}}} \frac{\Gamma(\alpha+2)}{\lambda_d^{\alpha+2}}.\end{aligned} \tag{A5}$$

b. *Growth of ice particles by vapor diffusion, assuming spherical shape*

In Figs. 8d,e and 10d,e, heating and cooling rates associated with the processes of deposition and sublimation are calculated by representing the crystals as simple spheres, such that the maximum dimension D as measured by the cloud probes is equal to their diameter. We now explain how these calculations are performed, starting with the bin scheme.

For the ice phase, the overall rate of change of mass due to deposition/sublimation, PRD (kg kg^{-1} s^{-1}), is computed in a similar fashion to Eq. (A3):

$$\mathrm{PRD} = \int_0^\infty N_I(D) \left.\frac{dm(D)}{dt}\right|_{\mathrm{dep}} dD, \tag{A6}$$

where $N_I(D)$ is the ice number concentration, and the rate of change of ice mass is given by

$$\left.\frac{dm(D)}{dt}\right|_{\mathrm{dep}} = \frac{4\pi C s_{\mathrm{ice}}}{AB_{\mathrm{ice}}} f_v. \tag{A7}$$

In Eq. (A7), C is the capacitance, a characteristic length scale used to represent the size and shape of ice crystals ($=0.5D$ for spherical ice), s_{ice} is the supersaturation with respect to ice, and

$$AB_{\mathrm{ice}} = \left[\frac{R_v T}{e_{\mathrm{ice}} D_V^*} + \frac{L_s}{TK_T^*}\left(\frac{L_s}{TR_v} - 1\right)\right], \tag{A8}$$

where e_{ice} is the saturation vapor pressure over ice and L_s is the latent heat of sublimation. Effects of ventilation on the rate of change of ice mass are accounted for by including the term f_v in the numerator of Eq. (A7), known as the ventilation coefficient. The magnitude of the ventilation coefficient is controlled by that portion of the particle's area most directly exposed to the oncoming flow, and thus depends on the particular geometry of the ice crystal. In Figs. 8d,e and 10d,e, the ventilation coefficient is calculated using the parameterization of Hall and Pruppacher (1976):

$$f_v = 1 + 0.14X^2, \quad \text{for} \quad X < 1.0, \tag{A9a}$$

$$f_v = 0.86 + 0.28X, \quad \text{for} \quad X \geq 1.0, \tag{A9b}$$

where $X = S_c^{1/3} R_e^{1/2}$. The Schimdt number S_c is defined as the ratio of the kinematic viscosity of air μ to the diffusivity of water vapor in air, D_V. The R_e is the Reynolds number, given by

$$R_e = \frac{VL^*}{\mu}, \tag{A10}$$

where V is the terminal velocity of the crystal and L^* is a length scale defined as Ω/P, where Ω is the total surface area of the crystal and P is the perimeter of the area projected normal to the direction of flow. For spherical ice, $L^* = D$.

Terminal velocities for ice crystals are assumed to obey a power-law relationship of the following form:

$$V(D) = a_s D^{b_s}, \tag{A11}$$

where coefficients $a_s = 11.72$ and $b_s = 0.41$ (for D in meters); these values are appropriate for "aggregates of unrimed radiating assemblages of plates, side planes, bullets and columns," following LH74.

In the bulk scheme, negative exponential functions are used to represent the number-size distribution for ice, such that $N(D) = N_{0\mathrm{i}} \exp(-\lambda_i D)$, where $N_{0\mathrm{i}}$ and λ_i are parameters that define the y intercept and slope of the negative exponential function respectively. Thus, Eq. (A6) becomes

$$\mathrm{PRD} = \frac{2\pi N_{0\mathrm{i}} s_{\mathrm{ice}}}{AB_{\mathrm{ice}}} \int_0^\infty D \exp(-\lambda_i D) f_v\, dD. \tag{A12}$$

Using the ventilation coefficient $f_v = 0.86 + 0.28 S_c^{1/3} R_e^{1/2}$ from Hall and Pruppacher (1976), in conjunction with Eqs. (A10) and (A11), we obtain

$$\mathrm{PRD} = \frac{2\pi N_{0i} s_{\mathrm{ice}}}{A B_{\mathrm{ice}}}\left[0.86\frac{\Gamma(2)}{\lambda^2} + 0.28\left(\frac{a_s}{\mu}\right)^{0.5} S_c^{1/3}(\rho_a\rho_0)^{0.25} \times \frac{\Gamma(0.5b_s + 2.5)}{\lambda^{0.5b_s+2.5}}\right], \tag{A13}$$

where ρ_a is the density of air and ρ_0 is the density of air at 850 hPa and 273.15 K.

c. *Growth of ice particles by vapor diffusion, accounting for ice crystal habit*

The heating and cooling rate calculations for profile 11 and run 15 are repeated using the bin scheme to account for the effects of ice crystal habit on the crystal growth rates; these results are shown in Figs. 13a and 13b. This is accomplished by choosing more appropriate values for the crystal capacitance C in Eq. (A7), based on a qualitative assessment of ice crystal habit from the cloud probe images. For profile 11 (Fig. 13a), the capacitance is obtained by representing the ice columns as spheroids of a given semiaxis length a (equal to the equatorial radius) and semiaxis length c (the distance from center to pole along the axis of symmetry). The ratio c/a of a spheroid defines its aspect ratio ϕ; prolate spheroids with $\phi > 1$ represent columns, while oblate spheroids with $\phi < 1$ represent planar crystals. For columns, $D = 2c$, and for plates, $D = 2a$. For profile 11, ϕ typically lay between 4 and 8, and this range was used to calculate corresponding values for the crystal capacitance following Pruppacher and Klett (1997). For run 15, which contains a mixture of pristine stellar crystals and aggregates, the capacitance is estimated to lie between $0.2D$ and $0.3D$, based on the results of Westbrook et al. (2008).

In terms of the effects of habit on ventilation, Westbrook and Heymsfield (2011) tested various parameterizations for f_v against laboratory data and showed that the use of Eq. (A9a), in conjunction with $L^* = D$ in Eq. (A10), is appropriate for planar and isometric crystals, but overestimates the ventilation coefficients for long columns and needles. Thus in Fig. 13a (profile 11), f_v was calculated using the more appropriate parameterization of Ji and Wang (1999):

$$f_v = 1.0 - 0.006\,68(X/4) + 2.394\,02(X/4)^2 + 0.734\,09(X/4)^3 - 0.739\,11(X/4)^4. \tag{A14}$$

In Fig. 13b (run 15), the Hall and Pruppacher coefficients [Eq. (A9a)] were used to calculate f_v. In both cases, the Reynolds number was calculated following Heymsfield and Westbrook (2010), which requires knowledge of the mass and area ratio of the crystals. The area ratio A_r is defined as the area of a particle projected normal to the flow divided by the area of a circumscribing disc. For profile 11, the area ratio of pristine crystals was calculated by treating the projected area of the columns as ellipses, and for run 15, where the pristine crystals are mainly stellars, we use $A_r = 0.5$ and $\phi = 0.01$. The images are also used to identify a size threshold D_{pristine}, above which aggregates appear to dominate the particle size distribution and below which only pristine crystals are assumed to exist. For profile 11, we used $D_{\mathrm{pristine}} = 1$ mm and for run 15, $D_{\mathrm{pristine}} = 0.6$ mm. For ice crystals whose maximum dimension D exceeds D_{pristine}, the mass and area ratio are assumed to obey a scaling law, based on the results of Schmitt and Heymsfield (2010). For a pristine ice crystal (i.e., for $D \le D_{\mathrm{pristine}}$), the mass is calculated from its volume $(4/3\pi a^3\phi)$ multiplied by an assumed value of the crystal density ρ_i. For profile 11, we used $\rho_i = 100\,\mathrm{kg\,m^{-3}}$ assuming hollow columns, and for run 15, $\rho_i = 500\,\mathrm{kg\,m^{-3}}$.

d. *Riming*

The mass growth rate of falling snow crystals due to the collection of cloud droplets (PSAC; $\mathrm{kg\,kg^{-1}\,s^{-1}}$) is parameterized in the bulk scheme following Morrison et al. (2005):

$$\mathrm{PSAC} = \frac{\pi N_{0i} a_s \Gamma(3 + b_s)\mathrm{ECI}\rho_a q_{\mathrm{liq}}}{4\lambda_i^{3+b_s}}\left(\frac{\rho_0}{\rho_a}\right)^{0.5}, \tag{A15}$$

where ECI = liquid-ice collection efficiency (equal to unity) and q_{liq} is the cloud liquid water mass mixing ratio. Equation (A15) is obtained by integrating the continuous collection equation (Pruppacher and Klett 1997) over the particle size distributions, using a simple gravitational collection kernel. Snowfall speed coefficients a_s and b_s are 11.72 and 0.41, respectively, as before; fall speeds for cloud droplets are assumed to be zero in this calculation.

REFERENCES

Bailey, M. P., and J. Hallett, 2009: A comprehensive habit diagram for atmospheric ice crystals: Confirmation from the laboratory, AIRS II, and other field studies. *J. Atmos. Sci.,* **66,** 2888–2899, doi:10.1175/2009JAS2883.1.

Bergeron, T., 1937: On the physics of fronts. *Bull. Amer. Meteor. Soc.,* **18,** 265–275.

Braun, S. A., and R. A. Houze, 1995: Melting and freezing in a mesoscale convective system. *Quart. J. Roy. Meteor. Soc.,* **121,** 55–77, doi:10.1002/qj.49712152104.

Browning, K. A., 1995: On the nature of the mesoscale circulations at a kata-cold front. *Tellus,* **47A,** 911–919, doi:10.1034/j.1600-0870.1995.00128.x.

——, and G. A. Monk, 1982: A simple model for the synoptic analysis of cold fronts. *Quart. J. Roy. Meteor. Soc.,* **108,** 435–452, doi:10.1002/qj.49710845609.

Chapman, D., and K. A. Browning, 1998: Use of wind-shear displays for Doppler radar data. *Bull. Amer. Meteor. Soc.,* **79,** 2685–2691, doi:10.1175/1520-0477(1998)079<2685:UOWSDF>2.0.CO;2.

Connolly, P. J., C. Emersic, and P. R. Field, 2012: A laboratory investigation into the aggregation efficiency of small ice crystals. *Atmos. Chem. Phys.,* **12,** 2055–2076, doi:10.5194/acp-12-2055-2012.

Cox, G. P., 1988: Modeling precipitation in frontal rainbands. *Quart. J. Roy. Meteor. Soc.,* **114,** 115–127, doi:10.1002/qj.49711447906.

Crosier, J., and Coauthors, 2014: Microphysical properties of cold frontal rainbands. *Quart. J. Roy. Meteor. Soc.,* **140,** 1257–1268, doi:10.1002/qj.2206.

Danard, M. B., 1964: On the influence of released latent heat on cyclone development. *J. Appl. Meteor.,* **3,** 27–37, doi:10.1175/1520-0450(1964)003<0027:OTIORL>2.0.CO;2.

Dearden, C., P. J. Connolly, T. W. Choularton, and P. R. Field, 2011: Evaluating the effects of microphysical complexity in idealised simulations of trade wind cumulus using the Factorial Method. *Atmos. Chem. Phys.,* **11,** 2729–2746, doi:10.5194/acp-11-2729-2011.

Doms, G., and Coauthors, 2007: A description of the nonhydrostatic regional COSMO model. Part II: Physical parameterization. Deutscher Wetterdienst, Offenbach, Germany, 154 pp. [Available online at http://www.cosmo-model.org/content/model/documentation/core/cosmoPhysParamtr.pdf.]

Forbes, R. M., and P. A. Clark, 2003: Sensitivity of extratropical cyclone mesoscale structure to the parametrization of ice microphysical processes. *Quart. J. Roy. Meteor. Soc.,* **129,** 1123–1148, doi:10.1256/qj.01.171.

Fridlind, A. M., A. S. Ackerman, G. McFarquhar, G. Zhang, M. R. Poellot, P. J. DeMott, A. J. Prenni, and A. J. Heymsfield, 2007: Ice properties of single-layer stratocumulus during the Mixed-Phase Arctic Cloud Experiment: 2. Model results. *J. Geophys. Res.,* **112,** D24202, doi:10.1029/2007JD008646.

Fukuta, N., and T. Takahashi, 1999: The growth of atmospheric ice crystals: A summary of findings in vertical supercooled cloud tunnel studies. *J. Atmos. Sci.,* **56,** 1963–1979, doi:10.1175/1520-0469(1999)056<1963:TGOAIC>2.0.CO;2.

Hall, W. D., and H. R. Pruppacher, 1976: Survival of ice particles falling from cirrus clouds in subsaturated air. *J. Atmos. Sci.,* **33,** 1995–2006, doi:10.1175/1520-0469(1976)033<1995:TSOIPF>2.0.CO;2.

Hallett, J., and S. C. Mossop, 1974: Production of secondary ice particles during riming process. *Nature,* **249,** 26–28, doi:10.1038/249026a0.

Harrington, J. Y., K. Sulia, and H. Morrison, 2013a: A method for adaptive habit prediction in bulk microphysical models. Part I: Theoretical development. *J. Atmos. Sci.,* **70,** 349–364, doi:10.1175/JAS-D-12-040.1.

——, ——, and ——, 2013b: A method for adaptive habit prediction in bulk microphysical models. Part II: Parcel model corroboration. *J. Atmos. Sci.,* **70,** 365–376, doi:10.1175/JAS-D-12-0152.1.

Heymsfield, A. J., and C. D. Westbrook, 2010: Advances in the estimation of ice particle fall speeds using laboratory and field measurements. *J. Atmos. Sci.,* **67,** 2469–2482, doi:10.1175/2010JAS3379.1.

Hobbs, P. V., and P. O. G. Persson, 1982: The mesoscale and microscale structure and organization of clouds and precipitation in midlatitude cyclones. Part V: The substructure of narrow cold-frontal rainbands. *J. Atmos. Sci.,* **39,** 280–295, doi:10.1175/1520-0469(1982)039<0280:TMAMSA>2.0.CO;2.

Hong, S. Y., J. Dudhia, and S. H. Chen, 2004: A revised approach to ice microphysical processes for the bulk parameterization of clouds and precipitation. *Mon. Wea. Rev.,* **132,** 103–120, doi:10.1175/1520-0493(2004)132<0103:ARATIM>2.0.CO;2.

Hoskins, B. J., M. E. McIntyre, and A. W. Robertson, 1985: On the use and significance of isentropic potential vorticity maps. *Quart. J. Roy. Meteor. Soc.,* **111,** 877–946, doi:10.1002/qj.49711147002.

Ji, W. S., and P. K. Wang, 1999: Ventilation coefficients for falling ice crystals in the atmosphere at low-intermediate Reynolds numbers. *J. Atmos. Sci.,* **56,** 829–836, doi:10.1175/1520-0469(1999)056<0829:VCFFIC>2.0.CO;2.

Joos, H., and H. Wernli, 2012: Influence of microphysical processes on the potential vorticity development in a warm conveyor belt: A case-study with the limited-area model COSMO. *Quart. J. Roy. Meteor. Soc.,* **138,** 407–418, doi:10.1002/qj.934.

Lackmann, G. M., 2002: Cold-frontal potential vorticity maxima, the low-level jet, and moisture transport in extratropical cyclones. *Mon. Wea. Rev.,* **130,** 59–74, doi:10.1175/1520-0493(2002)130<0059:CFPVMT>2.0.CO;2.

Lebo, Z. J., H. Morrison, and J. H. Seinfeld, 2012: Are simulated aerosol-induced effects on deep convective clouds strongly dependent on saturation adjustment? *Atmos. Chem. Phys.,* **12,** 9941–9964, doi:10.5194/acp-12-9941-2012.

Lloyd, G., C. Dearden, T. W. Choularton, J. Crosier, and K. N. Bower, 2014: Observations of the origin and distribution of ice in cold, warm, and occluded frontal systems during the DIAMET campaign. *Mon. Wea. Rev.,* doi:10.1175/MWR-D-13-00396.1, in press.

Locatelli, J. D., and P. V. Hobbs, 1974: Fallspeeds and masses of solid precipitation particles. *J. Geophys. Res.,* **79,** 2185–2197, doi:10.1029/JC079i015p02185.

Manabe, S., 1956: On the contribution of heat released by condensation to the change in pressure pattern. *J. Meteor. Soc. Japan,* **34,** 308–320.

Marécal, V., D. Hauser, and F. Roux, 1993: The 12/13 January 1988 narrow cold-frontal rainband observed during MFDP/FRONTS 87. Part II: Microphysics. *J. Atmos. Sci.,* **50,** 975–998, doi:10.1175/1520-0469(1993)050<0975:TJNCFR>2.0.CO;2.

Mason, B. J., 1994: The shapes of snow crystals—Fitness for purpose? *Quart. J. Roy. Meteor. Soc.,* **120,** 849–860, doi:10.1002/qj.49712051805.

Morrison, H., J. A. Curry, and V. I. Khvorostyanov, 2005: A new double-moment microphysics parameterization for application in cloud and climate models. Part I: Description. *J. Atmos. Sci.,* **62,** 1665–1677, doi:10.1175/JAS3446.1.

——, J. O. Pinto, J. A. Curry, and G. M. McFarquhar, 2008: Sensitivity of modeled arctic mixed-phase stratocumulus to cloud condensation and ice nuclei over regionally varying surface conditions. *J. Geophys. Res.,* **113,** D05203, doi:10.1029/2007JD008729.

Pruppacher, H. R., and J. D. Klett, 1997: *Microphysics of Clouds and Precipitation.* Springer, 954 pp.

Reisner, J., R. M. Rasmussen, and R. T. Bruintjes, 1998: Explicit forecasting of supercooled liquid water in winter storms using the MM5 mesoscale model. *Quart. J. Roy. Meteor. Soc.,* **124,** 1071–1107, doi:10.1002/qj.49712454804.

Rutledge, S. A., and P. V. Hobbs, 1983: The mesoscale and microscale structure and organization of clouds and precipitation in midlatitude cyclones. Part VIII: A model for the "seeder-feeder" process in warm-frontal rainbands. *J. Atmos. Sci.,* **40,** 1185–1206, doi:10.1175/1520-0469(1983)040<1185:TMAMSA>2.0.CO;2.

——, and ——, 1984: The mesoscale and microscale structure and organization of clouds and precipitation in midlatitude cyclones. Part XII: A diagnostic modeling study of precipitation

development in narrow cold-frontal rainbands. *J. Atmos. Sci.,* **41,** 2949–2972, doi:10.1175/1520-0469(1984)041<2949:TMAMSA>2.0.CO;2.

Sansom, H. W., 1951: A study of cold fronts over the British Isles. *Quart. J. Roy. Meteor. Soc.,* **77,** 96–120, doi:10.1002/qj.49707733111.

Schmitt, C. G., and A. J. Heymsfield, 2010: The dimensional characteristics of ice crystal aggregates from fractal geometry. *J. Atmos. Sci.,* **67,** 1605–1616, doi:10.1175/2009JAS3187.1.

Schultz, D. M., 2005: Review of cold fronts with prefrontal troughs and wind shifts. *Mon. Wea. Rev.,* **133,** 2449–2472, doi:10.1175/MWR2987.1.

Shampine, L. F., and M. W. Reichelt, 1997: The MATLAB ODE Suite. *SIAM J. Sci. Comput.,* **18,** 1–22, doi:10.1137/S1064827594276424.

Shipway, B. J., and A. A. Hill, 2012: Diagnosis of systematic differences between multiple parametrizations of warm rain microphysics using a kinematic framework. *Quart. J. Roy. Meteor. Soc.,* **138,** 2196–2211, doi:10.1002/qj.1913.

Skamarock, W. C., and Coauthors, 2008: A description of the Advanced Research WRF version 3. NCAR Tech. Note NCAR/TN-475+STR, 113 pp. [Available online at http://www.mmm.ucar.edu/wrf/users/docs/arw_v3_bw.pdf.]

Stoelinga, M. T., 1996: A potential vorticity-based study of the role of diabatic heating and friction in a numerically simulated baroclinic cyclone. *Mon. Wea. Rev.,* **124,** 849–874, doi:10.1175/1520-0493(1996)124<0849:APVBSO>2.0.CO;2.

Sulia, K. J., and J. Y. Harrington, 2011: Ice aspect ratio influences on mixed-phase clouds: Impacts on phase partitioning in parcel models. *J. Geophys. Res.,* **116,** D21309, doi:10.1029/2011JD016298.

——, ——, and H. Morrison, 2013: a method for adaptive habit prediction in bulk microphysical models. Part III: Applications and studies within a two-dimensional kinematic model. *J. Atmos. Sci.,* **70,** 3302–3320, doi:10.1175/JAS-D-12-0316.1.

Szeto, K. K., C. A. Lin, and R. E. Stewart, 1988a: Mesoscale circulations forced by melting snow. Part I: Basic simulations and dynamics. *J. Atmos. Sci.,* **45,** 1629–1641, doi:10.1175/1520-0469(1988)045<1629:MCFBMS>2.0.CO;2.

——, R. E. Stewart, and C. A. Lin, 1988b: Mesoscale circulations forced by melting snow. Part II: Application to meteorological features. *J. Atmos. Sci.,* **45,** 1642–1650, doi:10.1175/1520-0469(1988)045<1642:MCFBMS>2.0.CO;2.

Tonttila, J., E. J. O'Connor, S. Niemela, P. Raisanen, and H. Jarvinen, 2011: Cloud base vertical velocity statistics: A comparison between an atmospheric mesoscale model and remote sensing observations. *Atmos. Chem. Phys.,* **11,** 9207–9218, doi:10.5194/acp-11-9207-2011.

Vance, A. K., A. Woolley, R. Cotton, K. Turnbull, S. Abel, and C. Harlow, 2011: Final report on the WVSS-II sensors fitted to the FAAM BAe 146. Tech. Rep., Met Office, 24 pp.

Vaughan, G., and Coauthors, 2014: Cloud banding and winds in intense European cyclones: Results from the DIAMET project. *Bull. Amer. Meteor. Soc.,* doi:10.1175/BAMS-D-13-00238.1, in press.

Westbrook, C. D., and A. J. Heymsfield, 2011: Ice crystals growing from vapor in supercooled clouds between −2.5° and −22°C: Testing current parameterization methods using laboratory data. *J. Atmos. Sci.,* **68,** 2416–2429, doi:10.1175/JAS-D-11-017.1.

——, and A. J. Illingworth, 2011: Evidence that ice forms primarily in supercooled liquid clouds at temperatures >−27°C. *Geophys. Res. Lett.,* **38,** L14808, doi:10.1029/2011GL048021.

——, R. C. Ball, P. R. Field, and A. J. Heymsfield, 2004: Theory of growth by differential sedimentation, with application to snowflake formation. *Phys. Rev. E,* **70,** 021403, doi:10.1103/PhysRevE.70.021403.

——, R. J. Hogan, and A. J. Illingworth, 2008: The capacitance of pristine ice crystals and aggregate snowflakes. *J. Atmos. Sci.,* **65,** 206–219, doi:10.1175/2007JAS2315.1.

Wilson, D. R., and S. P. Ballard, 1999: A microphysically based precipitation scheme for the UK Meteorological Office Unified Model. *Quart. J. Roy. Meteor. Soc.,* **125,** 1607–1636, doi:10.1002/qj.49712555707.